Univerzita Karlova v Praze
Matematicko-fyzikální fakulta

DIPLOMOVÁ PRÁCE

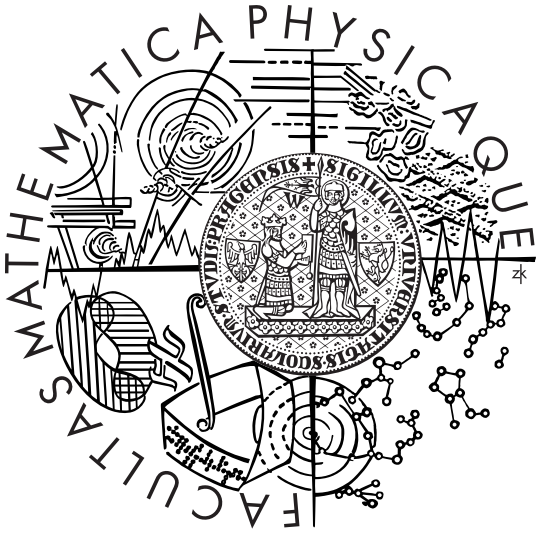

David Šálek

Studium produkce dijetů v difrakčních *ep* interakcích

Ústav částicové a jaderné fyziky
Vedoucí diplomové práce: RNDr. Alice Valkárová, DrSc.
Studijní program: Fyzika Mgr., Jaderná a částicová fyzika

Charles University in Prague
Faculty of Mathematics and Physics

DIPLOMA THESIS

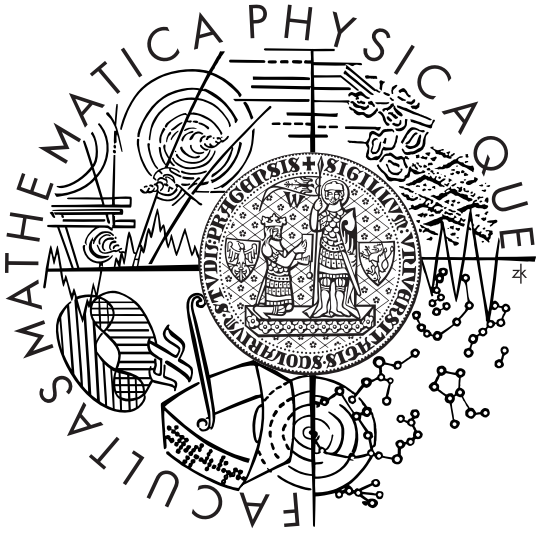

David Šálek

Dijet Production in Diffractive *ep* Interactions

Institute of Particle and Nuclear Physics
Supervisor: RNDr. Alice Valkárová, DrSc.
Master Degree in Physics, Nuclear and Particle Physics

Poděkování

Na tomto místě bych chtěl dostát své milé povinnosti a poděkovat Alici Valkárové za svědomité vedení - kdykoli jsem potřeboval pomoc, byla mi z její strany poskytnuta. Chvíle strávené konzultacemi nejrůznějších problémů a její lidský přístup mi byly tou největší inspirací a motivací k této práci. Děkuji i za vedení Proseminář z jaderné a subjaderné fyziky, jenž byl jedním z prvních impulsů, který ve mě vyvolal nadšení pro toto vědní odvětví.

Jsem vděčný za umožnění aktivního působení v mezinárodní vědecké komunitě na experimentu H1, za finanční i morální podporu při pobytech v zahraničí.

Jsem velmi zavázán Mirkovi Nožičkovi za nesmírnou pomoc v začátcích i za jeho cenné rady. Děkuji Richardovi Polifkovi za jeho společnost během uplynulých dvou let a plodné diskuse týkající se obou našich prací.

V neposlední řadě chci poděkovat Hannesovi Jungovi za odborné vedení a pomoc při nesnázích na analýze, která mi byla zadána na jeho doporučení.

Acknowledgements

At this place I would like to acquit my kind duty and express thanks to Alice Valkárová for her earnest supervision - whenever I needed she was always ready to help me. Time spent consulting various problems and her humane approach were the greatest inspiration and motivation for this work. I also thank for leading the Seminar of Nuclear and Particle Physics which was one of the first impulses that invoked my enthusiasm for this branch of science.

I am grateful for having the opportunity to take an active part in the international scientific communitiy at the H1 experiment and for the finantial and moral support during my stays abroad.

I am much obliged to Mirek Nožička for his immence help at the beginning and for all the valuable advices he has given me. I thank to Richard Polifka for his companionship during the last two years and for fruitful discussions concerning both our theses.

Not least I want to say thanks to Hannes Jung for his special guidance and for his help with the difficulties that have occured. This thesis was submitted to me on his recommendations.

Prohlašuji, že jsem svou diplomovou práci napsal samostatně a výhradně s použitím citovaných pramenů. Souhlasím se zapůjčováním práce.

V Praze dne David Šálek

What a meere child is Fancie,
That, having two faire gawdes of equall sweetnesse,
Cannot distinguish, but must crie for both.

William Shakespeare: The Two Noble Kinsmen, Act 4, Scene 2

Láska je dítě.
Jak uvidí dvě stejně krásné hračky,
neví, co chce, a domáhá se obou!

William Shakespeare: Dva vznešení příbuzní, Dějství 4., Scéna 2.[1]

[1]Translation by Martin Hilský.

Contents

Abstrakt

Existují dva různé přístupy k popisu difrakčních hluboce nepružných procesů: model dvougluonové výměny a model s rozloženým pomeronem. Zásadním rozdílem těchto dvou přístupů je azimutální asymetrie partonů, které se přemění v hadronový koncový systém. Případy v kinematické oblasti 4 GeV$^2 < Q^2 <$ 80 GeV^2, $0.05 < y < 0.7$, $x_{I\!P} < 0.05$, vykazující zřetelnou mezeru v rapiditách s $\eta_{max} < 3.2$ a obsahující alespoň dva jety rozvíjející se v oblasti pseudorapidity $-3 < \eta^* < 0$ v $\gamma^* p$ těžišťovém systému, s příčnou hybností $p_T^* > 3.5$ v tomtéž systému jsou srovnány s předpovědmi obou zmíněných modelů. Monte Carlo generátor RAPGAP je použit k tvorbě požadovaných vzorků případů. Analyzována jsou data nabraná v letech 1999, 2000.

Abstract

Two different approaches are available for the description of the diffractive deep-inelastic events: the two gluon exchange model and the resolved pomeron model. The azimuthal asymmetry of the partons which transform into the hadronic final state is the major difference of these two approaches. Events in the kinematic region of 4 GeV$^2 < Q^2 <$ 80 GeV^2, $0.05 < y < 0.7$, $x_{I\!P} < 0.05$, exhibiting a clear rapidity gap with $\eta_{max} < 3.2$, and containing at least two jets evolving in the range of pseudorapidity $-3 < \eta^* < 0$ in the $\gamma^* p$ centre-of-mass system, with the transverse momenta $p_T^* > 3.5$ in the same system are compared with the predictions of both mentioned models. RAPGAP Monte Carlo generator is used to produce required event samples. Data acquired in the years 1999, 2000 are analysed.

Chapter 1

Introduction

Since the end of the 1960s, deep-inelastic scattering of leptons on stationary targets has been of great importance in elucidating the structure of the proton and neutron. The point-like electron or muon serves as a 'clean' probe, the final state being easier to interpret than that resulting from a hadron-hadron collision. Successive generations of accelerators have provided lepton beams at higher and higher energies, allowing smaller and smaller scales to be probed, but the attainable energy has been limited by the problem of energy loss through synchrotron radiation. The *ep* collider HERA, which began running in 1992, sidesteps this difficulty by using a high-momentum beam of protons instead of a stationary target. The result is a leap of an order of magnitude in centre-of-mass energy, increasing the accessible Q^2 by approximately two orders of magnitude and pushing the lower limit of x down by a similar factor.

One surprising feature of the HERA data is the existence of a significant fraction of deep-inelastic events in which there is a large angle between the proton remnant and the nearest particle - a *rapidity gap*. These events are termed *diffractive*, and seem to be related to similar processes which occur in photoproduction and have been observed in hadron-hadron interactions for some time. The presence of a gap indicates that a colourless object is exchanged, so there is no string of colour flux linking the two parts of the hadronic final state. These exchanges are successfully described in hadron-hadron interactions by *Regge theory*, according to which the dominant effect at high energies is exchange of the *pomeron* - an object with the quantum numbers of the vacuum. Despite the success of Regge theory, and its application to total cross sections and hence to the rise of F_2 at small x, there is no clear picture of how the pomeron arises from QCD, the fundamental theory of strong interactions.

The simplest picture of a pomeron as an object formed by the fundamental building blocks - quarks and gluons - is the one including two gluons only. Then the diffractive processes are mediated by the *two gluon exchange*

and no phenomenological object, such as pomeron, is present. Thus two different approaches are available for the description of the diffractive deep-inelastic events: the two gluon exchange model and the resolved pomeron model.

In this thesis, dijet production in diffractive deep-inelastic scattering is investigated in purpose of deciding in favour of one of the models. Jets conserve the direction of the original partons, hence can be used to study their angular dependencies. The azimuthal asymmetry obtained from the calculations is the major difference of the two approaches, and it is the main aim of this analysis to compare the both predictions with the azimuthal distribution exposed by real data.

Chapter 2

Deep-Inelastic Scattering and QCD

2.1 Kinematics of Deep-Inelastic Scattering

In figure 2.1, the kinematics of deep-inelastic electron-proton scattering are visualised. The beam electron interacts with a parton from the proton by the exchange of a virtual gauge boson. In neutral current (NC) scattering, a γ^* or Z^0 boson is exchanged. In the case of charged current (CC) scattering, a $W^\pm$ boson is exchanged, which leads to an electron-neutrino in the final state. If the 4-vector of the incoming and outgoing lepton are denoted k and k' and q is the boson 4-vector, the negative squared invariant mass of the exchanged virtual boson is given by

$$Q^2 = -q^2 = (k - k')^2. \tag{2.1}$$

Values of Q^2 above $\approx 4\ \mathrm{GeV}^2$ correspond to the regime of deep-inelastic scattering. If the photon is almost real ($Q^2 \simeq 0$), the process is usually referred to as *photoproduction*. It is convenient to introduce the two dimensionless quantities x and y:

$$x = \frac{-q^2}{2P \cdot q} \qquad (0 \leq x \leq 1), \tag{2.2}$$

$$y = \frac{P \cdot q}{P \cdot k} \qquad (0 \leq y \leq 1), \tag{2.3}$$

where P denotes the 4-vector of the proton. The squared invariant masses of the electron-proton and photon-proton systems s and W^2 are given by[1]:

$$s = (k + P)^2 \simeq Q^2/xy \simeq 4E_e E_p, \tag{2.4}$$

$$W^2 = (q + P)^2 \simeq ys - Q^2. \tag{2.5}$$

[1]Particle masses have been neglected.

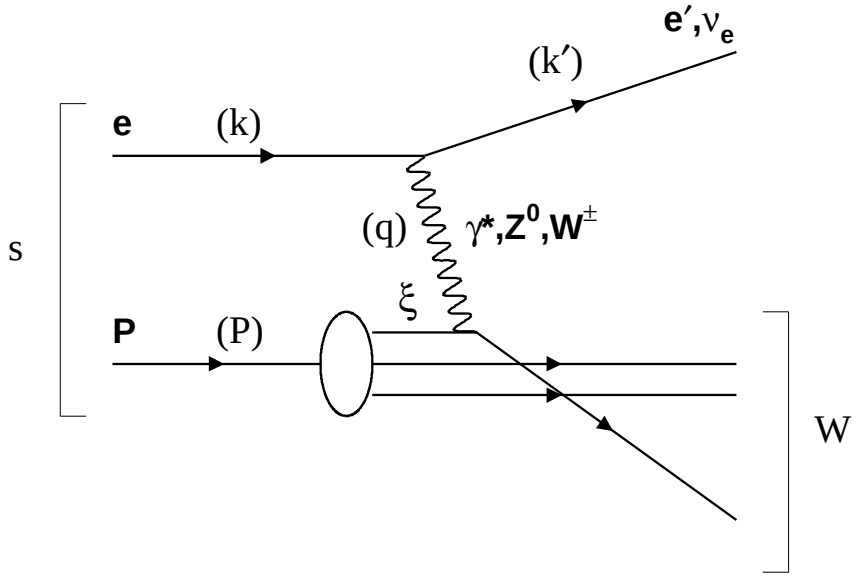

Figure 2.1: The kinematics of deep-inelastic electron-proton scattering. The electron (with 4-vector k) interacts with the proton (P) via the exchange of a virtual gauge boson (q), which scatters off a parton in the proton with longitudinal momentum fraction ξ.

2.2 DIS Cross Section and Parton Model

The analysis presented in this thesis is only concerned with neutral current (NC) interactions. The deep-inelastic scattering cross section can then be expressed as the sum of the contributions from γ^* and Z^0 exchange and an interference term:

$$\sigma_{NC} = \sigma(\gamma^*) + \sigma(Z^0) + \sigma(\gamma^* Z^0). \tag{2.6}$$

The large mass of the Z^0 boson[2] suppresses the contribution from Z^0 exchange and the interference term at low values of Q^2 according to the ratios of the propagator terms:

$$\frac{\sigma(Z^0)}{\sigma(\gamma^*)} \sim \left(\frac{Q^2}{Q^2 + M_Z^2}\right)^2, \qquad \frac{\sigma(\gamma^* Z^0)}{\sigma(\gamma^*)} \sim \frac{Q^2}{Q^2 + M_Z^2}. \tag{2.7}$$

Since in the analysis presented here deep-inelastic scattering events for $Q^2 < 80$ GeV^2 are studied, the contributions from Z^0 exchange and $Z^0\gamma^*$-interference can safely be neglected. The cross section, expressed in terms

[2] $M_{Z^0} = 91.1876 \pm 0.0021$ GeV [23]

of the two variables x and Q^2, can then be written as:

$$\frac{d^2\sigma(x,Q^2)}{dxdQ^2} = \frac{4\pi\alpha^2}{xQ^4}\left[\left(1-y+\frac{y^2}{2}\right)F_2(x,Q^2) - \frac{y^2}{2}F_L(x,Q^2)\right], \quad (2.8)$$

where α is the electromagnetic coupling and $F_2(x,Q^2)$ denotes the proton structure function. Because the cross section consists of two contributions from the scattering of transversally and longitudinally polarised photons, the longitudinal structure function $F_L(x,Q^2)$ is introduced. F_2 corresponds to the sum of longitudinal and transverse photon polarisation contributions, whereas F_L corresponds to longitudinal polarisation only. The ratio of the longitudinal to transverse photon cross sections $R(x,Q^2)$ is given by

$$R(x,Q^2) = \frac{\sigma_L}{\sigma_T} = \frac{F_L(x,Q^2)}{F_2(x,Q^2) - F_L(x,Q^2)}. \quad (2.9)$$

The DIS cross section can be then re-expressed as:

$$\frac{d^2\sigma(x,Q^2)}{dxdQ^2} = \frac{4\pi\alpha^2}{xQ^4}\left[1-y+\left(\frac{1}{1+R}\right)\frac{y^2}{2}\right]F_2(x,Q^2). \quad (2.10)$$

In the kinematic region of not too large y, contributions from longitudinal photon exchange can be neglected ($R=0$) and the last equation reduces to

$$\frac{d^2\sigma(x,Q^2)}{dxdQ^2} = \frac{4\pi\alpha^2}{xQ^4}\left(1-y+\frac{y^2}{2}\right)F_2(x,Q^2). \quad (2.11)$$

2.3 The Parton Model

When the first deep-inelastic scattering experiments were performed at SLAC, a *scaling* behaviour of the proton structure function was observed: $F_2(x,Q^2)$ was found to be approximately independent of Q^2 for $1 < Q^2 < 10$ GeV^2. Bjorken [15] predicted that F_2 should only depend on x in the limit $Q^2 \to \infty$. The quark-parton model, invented by Feynman [16] to explain the scaling behaviour, is based on two assumptions:

- The hadron taking part in the scattering process is made of point-like constituents (partons or *quarks*, as introduced by Gell-Mann [17]), among which the hadron momentum is distributed.
- At large Q^2, the quarks interact as free particles inside the hadron. At the short time scale $\mathcal{O}(1/\sqrt{Q^2})$ of the interaction, the photon sees a frozen state of non-interacting quarks. The cross section can thus be expressed as an incoherent sum of elastic photon-parton scattering processes.

In the parton model, the dimensionless quantity x corresponds to the momentum fraction ξ of the struck quark (neglecting the quark mass). In consequence, the structure function F_2 can be expressed as:

$$F_2(x, Q^2) \rightarrow F_2(x) = \sum_i e_i^2 x f_i(x). \tag{2.12}$$

Here, the sum runs over the constituent quarks, e_i is the electric charge of quark i and $f_i(x)$ is the momentum distribution or *parton density* function in the proton. If quarks and anti-quarks were the only constituents of the proton, their momentum sum should be equal to unity. Measurements however yield $\sum_i \int_0^1 x[q(x) + \bar{q}(x)]dx \simeq 0.5$. The missing momentum is carried by gluons.

2.4 Quantum Chromodynamics

With more and more precise structure function measurements, *scaling violations*, i.e. a dependence of F_2 on Q^2, are observed at x values lower and higher than those accessed by the first SLAC measurements. F_2 exhibits a dependence on the resolution power Q^2 of the photon probe. These *scaling violations* can be explained within Quantum Chromodinamics (QCD): The quarks in the proton can radiate qluons which themselves may split into $q\bar{q}$ pairs.

QCD is a non-Abelian gauge theory which is invariant under $SU(3)$ *colour* transformation. Colour corresponds to an additional degree of freedom which represents the charge of the strong interaction. The colour charge is carried by quarks and gluons. Quarks appear in *red*, *green* or *blue* colour. The massless gauge bosons of the theory are the eight bi-coloured gluons. The qluon self-coupling is a reflection of the non-Abelian structure of QCD.

2.4.1 Renormalisation

To calculate QCD cross sections, integrations have to be performed over the entire phase space of real and virtual quarks and gluons. These integrals turn out to be divergent. A scheme called *regularization* is therefore defined to leave out the divergent parts of the integrals. The calculated cross sections then depend on the energy scale μ_r^2 used in the regularization. This dependence is compensated by defining an effective coupling constant α_s, in which the divergent contributions are absorbed, so-called *renormalization*. The coupling constant is defined by the renormalization scheme used and depends on the *renormalization scale* μ_r^2. The requirement that the calculated cross sections should be independent of μ_r^2 leads to the renormalization group equations (RGE), a perturbative expansion in α_s which describes the

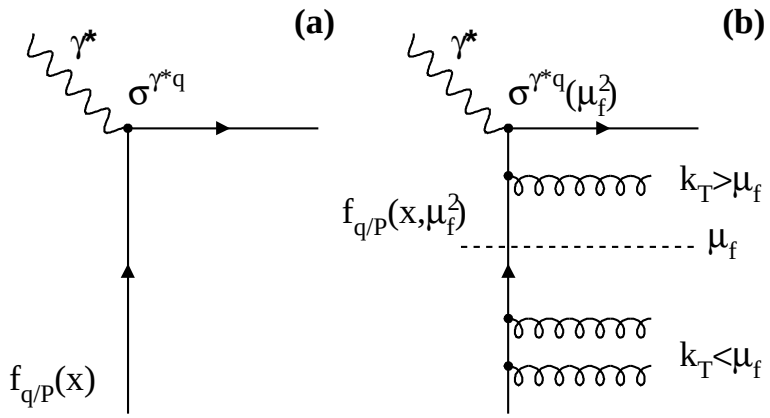

Figure 2.2: Hard scattering factorisation in QCD. Diagrams for photon-quark scattering *(a)* in lower order and *(b)* in higher orders of α_s are shown. By a redefinition of the quark distribution function $f_{q/P}$ all soft gluon emissions with transverse momentum $k_T < \mu_f$ are absorbed into the quark density (k_T is the gluon transverse momentum with respect to the proton). This introduces a dependence on the factorisation scale μ_f into both the quark density $f_{q/P}(x, \mu_f^2)$ and the partonic cross section $\sigma^{\gamma^* q}(\mu_f^2)$ of the process.

dependence of α_s on μ_r^2. Performing the calculation up to $\mathcal{O}(\alpha_s)$ one gets:

$$\alpha_s(\mu_r^2) = \frac{12\pi}{(33 - 2n_f)\ln(\mu_r^2/\Lambda_{QCD}^2)}. \tag{2.13}$$

Here, Λ_{QCD} is a free parameter which has to be determined experimentally and n_f is the number of quarks with mass less then μ_r. The scale dependence of the strong coupling constant has the following consequences:

- Asymptotic freedom: For higher values of μ_r^2 the coupling α_s decreases so that cross sections for specific processes are calculable as a perturbative expansion in α_s. In this limit quarks can be treated as free particles.

- Infrared slavery: At small values of μ_r^2, corresponding to large distances, the coupling strength α_s gets large and perturbative theory is no longer applicable. Quarks are confined in hadrons and non-perturbative methods have to be applied.

2.4.2 Factorisation

The theorem of *hard scattering factorisation in QCD* states that the short-range, perturbatively calculable aspects of a physical process can be separated from the long-range aspects, for which perturbation theory is not applicable. As an application of this theorem, the proton structure function F_2 can be expressed as:

$$F_2(x, Q^2) = \sum_{i=q,g} \int_x^1 d\xi f_i(\xi, \mu_r^2, \mu_f^2, \alpha_s) \cdot C_i^V \left(\frac{x}{\xi}, \frac{Q^2}{\mu_r^2}, \mu_f^2, \alpha_s \right). \qquad (2.14)$$

Here, μ_f^2 is the *factorisation scale*, the C_i^V are *coefficient functions* and f_i are the parton distribution functions. The factorisation scale μ_f^2 defines the energy scale above which the process is calculated within perturbative QCD (see figure 2.2). The resulting coefficient functions C_i^V depend on the parton flavour i and on the exchanged boson V, but *not* on the type of hadron. They are therefore process independent. The physics below the factorisation scale is absorbed into the quark and gluon distribution functions f_i, which are dependent on the hadron which takes part in the interaction.

Because the coefficient functions have been calculated completely so far only up to $\mathcal{O}(\alpha_s^2)$ for the inclusive ep cross section, the calculated cross sections as well as the parton distribution functions exhibit dependences on the choices of the renormalization and factorisation scales.

Chapter 3

Diffractive Scattering and the Pomeron

Events with a large rapidity gap - a region free of hadrons between the proton remnant and the current region - have been observed both in photoproduction [3, 4, 5, 6], and in DIS [7, 8] at HERA. Such events are explained as being due to the exchange of a colourless object, so that there is no string of colour field connecting the two parts of the hadronic final state and filling the gap by hadronization. Similar diffractive events have been observed for decades in hadron-hadron collisions, but there is no agreed mechanism for them in terms of QCD. They are, however, well described by *Regge theory* [9] - the phenomenological model of colourless exchanges between hadrons, which predates QCD. DIS at HERA offers a new way of probing the partonic structure of the diffractive exchange and thus distinguishing between various models that have been proposed.

3.1 Deep-Inelastic Scattering

Deep-Inelastic events with a rapidity gap in the forward direction have been observed by both ZEUS [7] and H1 [8] (see figure 3.1). These indicate a colour-singlet exchange between the virtual photon and the proton, which is scattered elastically or dissociates into a low-mass state and is lost in the beam pipe.

The scattered proton, which has a very small transverse momentum $p_\perp \approx \sqrt{t}$, could not be detected using the H1 detector. Instead, the presence of a rapidity gap extending up to the beam pipe is used as a signature of diffractive exchange. This is quantified using the variable η_{max}, defined as the *pseudorapidity*

$$\eta = -\ln\left(\tan\frac{\theta}{2}\right) \tag{3.1}$$

of the most forward energy deposit of more than 400 MeV. A small η_{max}

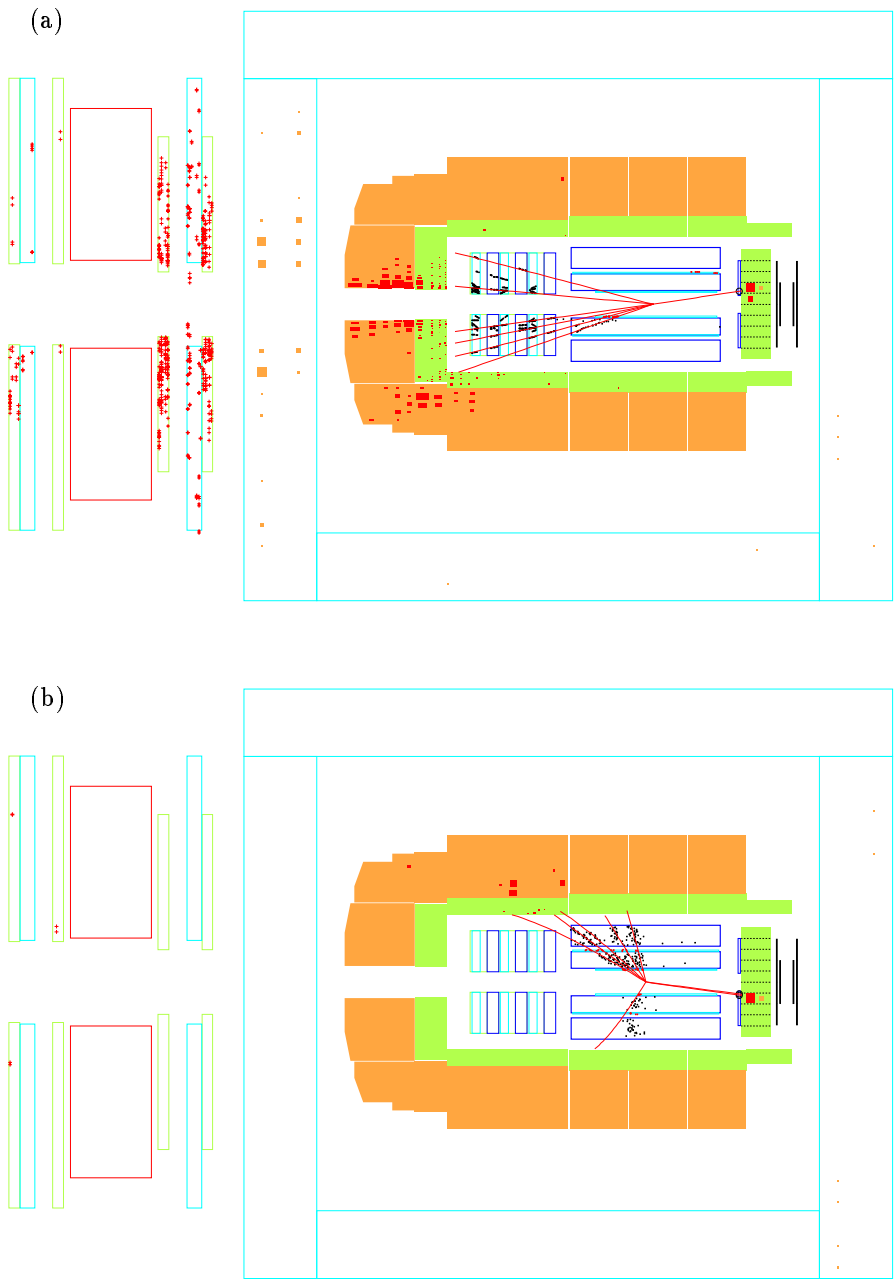

Figure 3.1: *(a)* A 'standard' deep-inelastic event with no rapidity gap, as seen in the H1 detector. *(b)* A deep-inelastic event with a rapidity gap, as seen in the H1 detector.

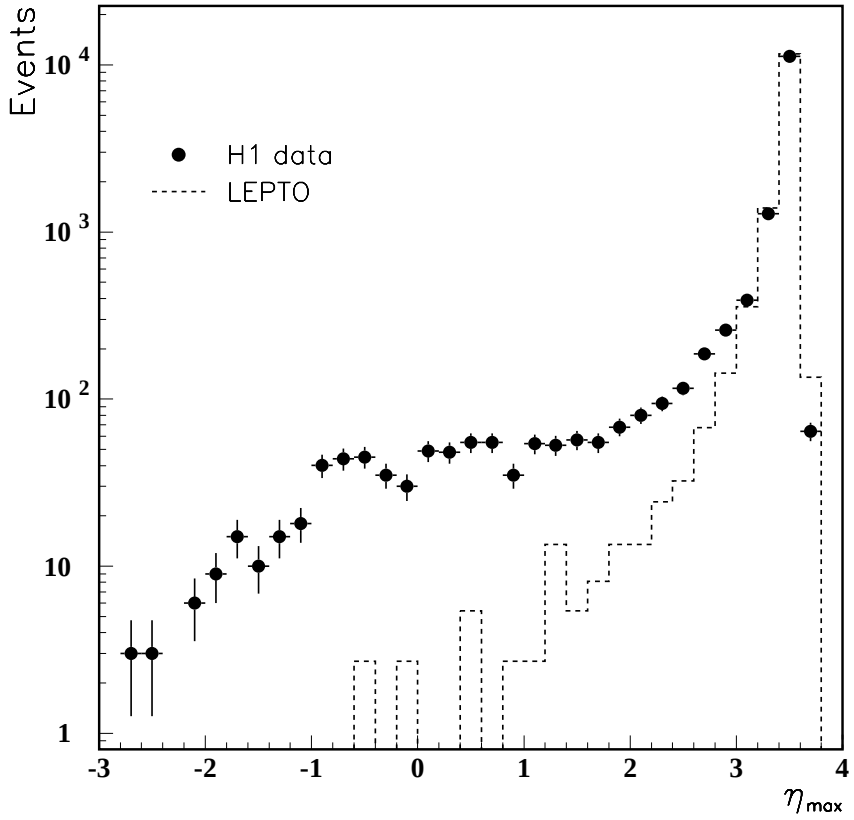

Figure 3.2: Distribution of measured η_{max} for DIS events, compared with the expectation of a 'standard DIS' model (LEPTO).

indicates a large rapidity gap. The number of events with large rapidity gaps is much greater than predicted by a 'standard DIS' Monte Carlo generator, which produces large rapidity gaps only as rare statistical fluctuations in the hadronization process (see figure 3.2).

Figure 3.3 shows a schematic diagram of a typical diffractive event. It demonstrates the basic properties of the phenomenological model of colourless exchange already mentioned in the beginning of this chapter. The so-called Regge theory describes the diffraction by means of an exchanged object, referred to as *pomeron*, matching none of the known mesons. Pomeron carries the quantum numbers of the vacuum, which is reflected in a rapidity gap observed in the diffractive processes. The diffractive system X and the proton-remnant system Y are spatially separated due to absence of the colour flow caused by the exchange of the colourless object.

The clear separation of the hadronic final state into two systems X and

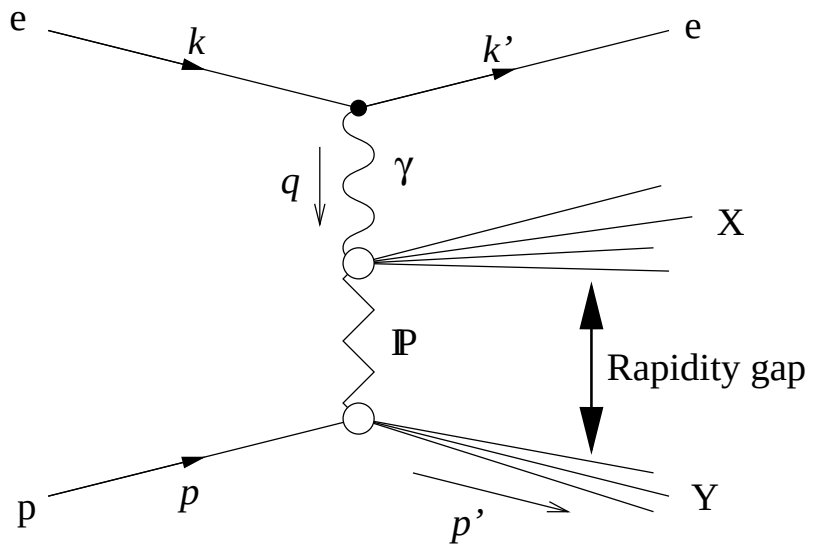

Figure 3.3: A schematic diagram of the process with a large rapidity gap.

Y allows three further kinematic quantities to be defined, in addition to those used in standard DIS (section 2.1):

$$t = (p - p')^2 \tag{3.2}$$

$$\beta = \frac{Q^2}{Q^2 + M_X^2} \tag{3.3}$$

$$x_{I\!P} = \frac{Q^2 + M_X^2}{Q^2 + W^2}. \tag{3.4}$$

The Mandelstam variable t is the squared four-momentum carried by the colour-singlet exchange (the pomeron in the Regge picture). The variables β and $x_{I\!P}$ are analogous to x and y. Like x for the proton, β is the fraction of the momentum of the pomeron going into the hard subprocess (interacting with the virtual photon). In the limit $t \to 0$, $x_{I\!P}$ is the fraction of the momentum of the proton carried away by the pomeron.

The contribution of diffractive events with an elastically scattered proton can be quantified by defining a diffractive structure function $F_2^{D(4)}$, analogous to the inclusive proton structure function F_2:

$$\frac{d^4\sigma_{ep\to epX}}{dx dQ^2 dx_{I\!P} dt} =$$

$$= \frac{4\pi\alpha^2}{xQ^4}\left\{1 - y + \frac{y^2}{2[1 + R^{D(4)}(x, Q^2, x_{I\!P}, t)]}\right\} F_2^{D(4)}(x, Q^2, x_{I\!P}, t). \tag{3.5}$$

If t cannot be experimentally retrieved the measured cross section is actually an integral over t up to $|t| \approx 1$ GeV^2. This limit is determined by the requirement that the proton remnant is not detected. The ratio of the cross sections for diffractive processes due to longitudinally and transversally polarised photons, $R^{D(4)}$, is not well measured and its value makes only a small difference to $F_2^{D(4)}$, so it is set to zero for the measurement made by H1 [13, 14] of the structure function $F_2^{D(3)}$, defined by

$$\frac{d^3\sigma_{ep\to epX}}{dxdQ^2dx_{I\!P}} = \frac{4\pi\alpha^2}{xQ^4}\left\{1 - y + \frac{y^2}{2}\right\} F_2^{D(3)}(x, Q^2, x_{I\!P}). \tag{3.6}$$

Some models, such as that of Ingelman and Schlein [10], feature a factorisable diffractive structure function

$$F_2^{D(3)} = F_2^{I\!P}(\beta, Q^2) \cdot f_{I\!P/p}(x_{I\!P}) \tag{3.7}$$

where $F_2^{I\!P}$ is the structure function of the pomeron and the *flux factor* $f_{I\!P/p}$ describes the pomeron content of the proton. This makes sense in a picture where the pomeron is a hadronic object that is emitted by the proton and then probed by the virtual photon in a hard interaction. Although initial results [13] were consistent with factorisation, a more recent study using higher statistics [14] shows that factorisation in this simple form does not hold. This may simply be because there is a contribution at larger $x_{I\!P}$ from meson exchange; as results are consistent with the sum of two individually factorisable components - one from a meson trajectory and one from pomeron exchange. However, it may be that even the purely diffractive (pomeron exchange) component does not factorise due, for example, to multiple pomeron exchange, or to a failure of the picture of the pomeron as a particle-like object.

The nearest practically measurable quantity to the pomeron structure function $F_2^{I\!P}$ is the integral of the diffractive structure function $F_2^{D(3)}$ over the available range of $x_{I\!P}$:

$$\tilde{F}_2^{D(3)}(\beta, Q^2) = \int_{x_{I\!P_L}}^{x_{I\!P_H}} F_2^{D(3)}(\beta, x_{I\!P}, Q^2) dx_{I\!P}. \tag{3.8}$$

The results obtained by H1 [14] are shown in figure 3.4. Even if factorisation does not hold to high precision, $\tilde{F}_2^D$ provides a measure of the 'average' deep-inelastic structure of the diffractive exchange. If $F_2^{D(3)}$ is treated as the sum of two factorisable components, $\tilde{F}_2^D$ may be extracted from the separated pomeron component, or by using the total $F_2^{D(3)}$ in a region where $x_{I\!P}$ is small enough for the meson component to be small. The two methods give compatible results. The 'pomeron structure function' $\tilde{F}_2^D$ shows a logarithmic rise with Q^2, like the proton structure function F_2, consistent with a partonic structure for the pomeron. The fact that this rise with Q^2 is

present up to fairly large values of β suggests a structure of valence gluons; hadrons, with their valence quark structure, show a decrease with Q^2 at high x, due to the valence quarks losing momentum by radiating gluons.

If the pomeron is treated as a hadronic object, its quark and gluon content can be obtained using a QCD-based fit to the diffractive function $\tilde{F}_2^D$ [14]. The result is a structure in which 80% of the momentum of the pomeron is carried by gluons, which are strongly peaked near $\beta = 1$ at $Q^2 = 2.5$ GeV^2, the scale used for the DGLAP evolution. In other words, at this scale the momentum of the pomeron is often carried almost entirely by a single gluon. At higher Q^2, QCD evolution spreads the distribution more evenly over the available range in β. The β distributions at two different values of Q^2 are shown in figure 3.5.

3.2 Models of Hard Diffraction

3.2.1 Ingelman and Schlein

A lot of work on the phenomenology of diffractive interactions is based on the idea of *factorisation*, meaning that the cross section for a hard diffractive process (such as jet production in hadron-hadron collisions or DIS at HERA) is treated as the product of a non-perturbative (soft) factor describing the emission of a pomeron by the proton, and a perturbative factor describing the hard interaction of a parton from the pomeron with a virtual photon or a parton from the other hadron. If this approach is valid, there must be a universal structure function for the pomeron, $F_2^{I\!P}$, which applies in DIS, in hard photoproduction and in hadron-hadron interactions. The pomeron structure function can be related to a set of hypothetical quarks and gluons distributions in the pomeron in the same way as the proton structure function F_2 is related to the quark and gluon content of the proton. In this picture, the pomeron is treated more or less as a particle, although it is only detected as a t-channel exchange, with a negative four-momentum squared.

This approach was suggested by Ingelmann and Schlein [10], who used it to predict the production of jets in diffractive pp scattering, later confirmed at UA8 [11, 12]. They used two different pomeron structures, both dominated by gluons but with a hard distribution $xG(x) = 6x(1-x)$ in one case and a soft distribution $xG(x) = 6(1-x)^5$ in the other. Using the particle-like structure of the pomeron, they imposed a momentum sum rule $\int_0^1 xG(x)dx = 1$ to fix the normalisation of the gluon distribution.

3.2.2 The Two Gluon Exchange Model

The two gluon exchange model allows a fully perturbative QCD approach to diffraction. A basic Feynman diagram of this mechanism is depicted in

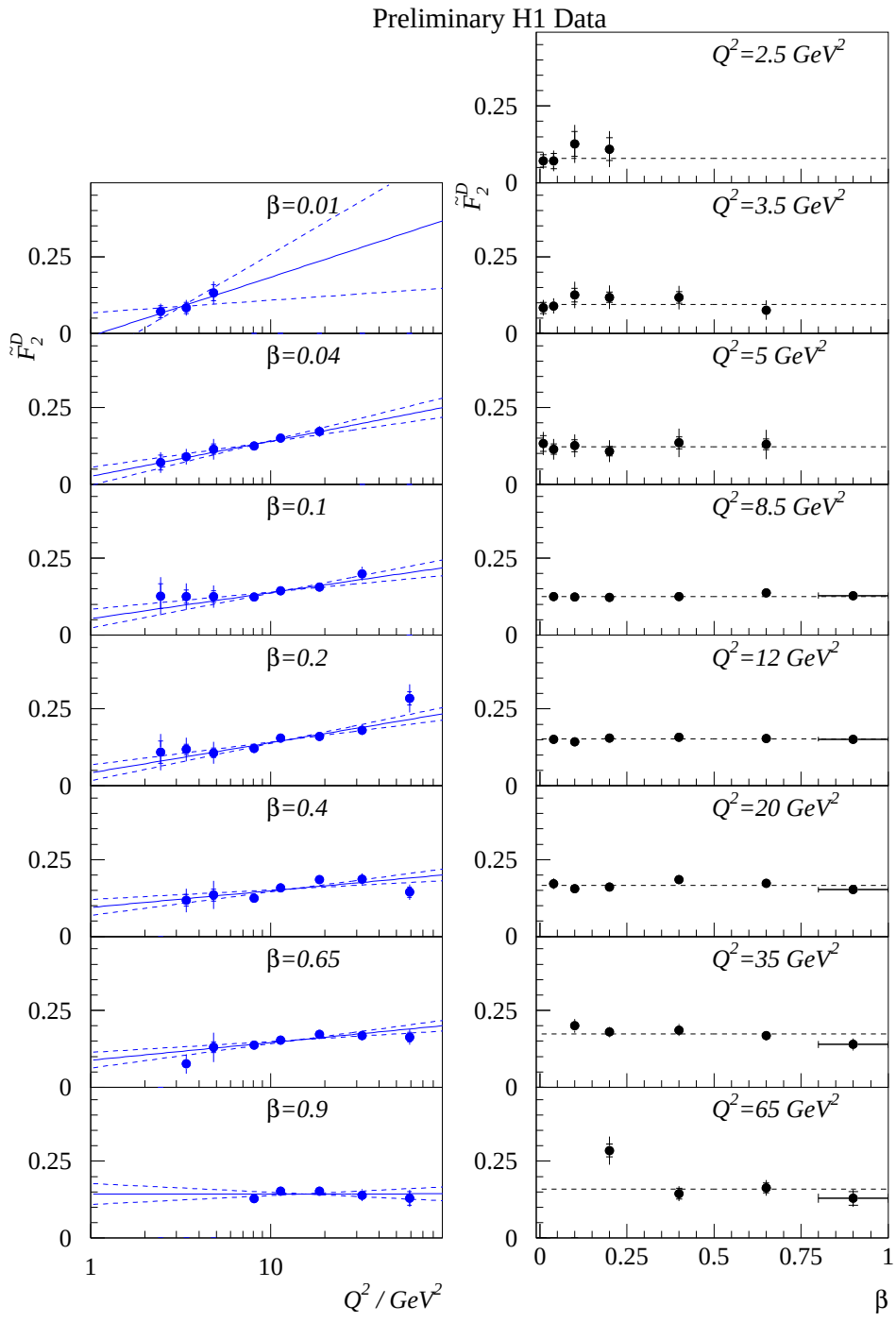

Figure 3.4: The structure function $\tilde{F}_2^{D(3)}(\beta, Q^2)$ as a function of Q^2 for different values of β (left) and as a function of β for different values of Q^2 (right). Taken from [14].

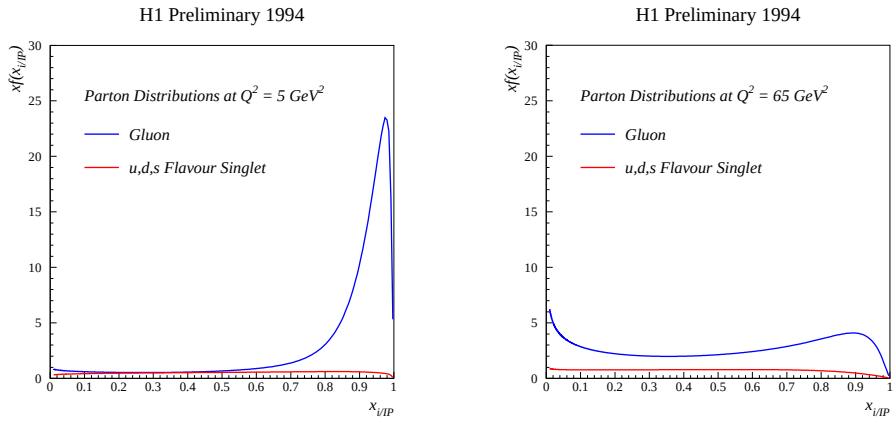

Figure 3.5: Gluon and quark distributions in the pomeron, extracted from a QCD-based fit to $F_2^{D(3)}$: *(a)* at low Q^2, showing the large contribution from gluons near $\beta = 1$; *(b)* at higher Q^2, after evolution to smaller β. Taken from [14].

figure 3.6. The quark and the antiquark emerging from the lepton vertex are coupled to one gluon each. These gluons are determined by the gluon densities in the proton.

Since both the quark and the antiquark participate in the hard interaction, they both receive the same transverse momentum in the $\gamma^* p$ centre-of-mass system, without producing a remnant, and both final state partons are allowed to further radiate partons in the final state parton shower. This has to be contrasted to the resolved pomeron model, where also a $q\bar{q}$ final state appears in a QPM process, but there the quarks have vanishing transverse momentum in the $\gamma^* p$ frame and a pomeron remnant is present.

The pQCD calculation of diffraction is applicable mainly to exclusive high p_T di-jet production. [19, 20] There is another process within the pQCD approach that has to be taken into account. It is derived from the one displayed in figure 3.6, and includes an additional gluon radiated from one of the exchanged gluons. This gluon contributes to the final state along with the quark-antiquark pair. [21]

3.3 Dijet Production

In case of the two gluon exchange model it is quite clear how the two jets emerge. Concerning the $q\bar{q}$ process the jets rise from the quark and the antiquark each. The same situation is in case of the $q\bar{q}g$ process provided that the gluon is collinear with one of the quarks. If a harder gluon is

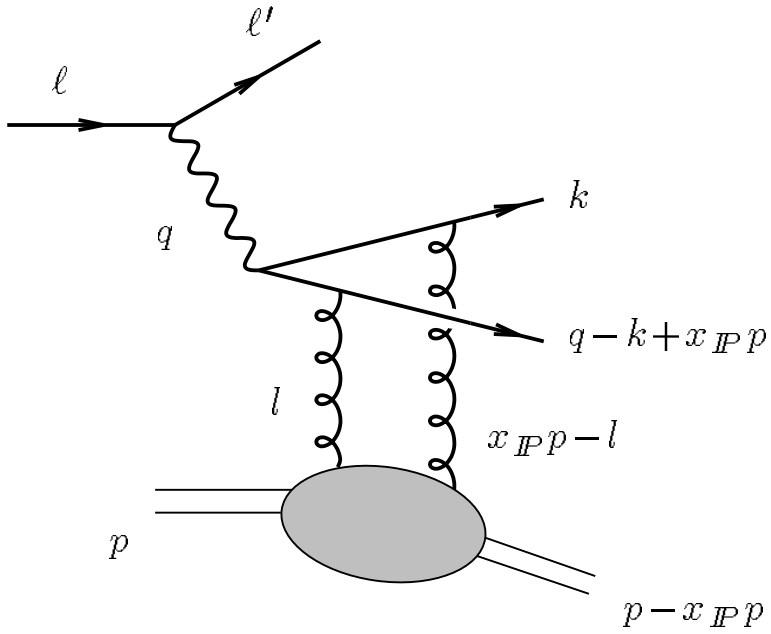

Figure 3.6: The two gluon exchange mechanism.

radiated then one jet stems out of it, whereas the other jet emerges from the two quarks and evolves counterwise the gluon direction in $\gamma^* p$ centre-of-mass system.

The situation in the resolved pomeron model requires more detailed study. A basic process concerning an exchange of a pomeron is so-called *quark parton model process* depicted in figure 3.7. It is a process of the order α_{em} only, where a gluon originating from the pomeron interacts with the virtual photon. Such process contributes to the dijet production since there is also a pomeron remnant forming the hadronic final state X. But the dominant processes responsible of the dijet production are of the order $\alpha_{em}\alpha_s$.

3.3.1 Order $\alpha_{em}\alpha_s$ Processes

At $\mathcal{O}(\alpha_{em}\alpha_s)$, the following diagrams have to be included in the calculation of the DIS cross section in addition to the bare quark parton model (QPM) process (see figure 3.7):

- QCD-Compton Scattering (QCDC): The struck quark from the proton radiates a gluon before or after the interaction with the virtual photon;

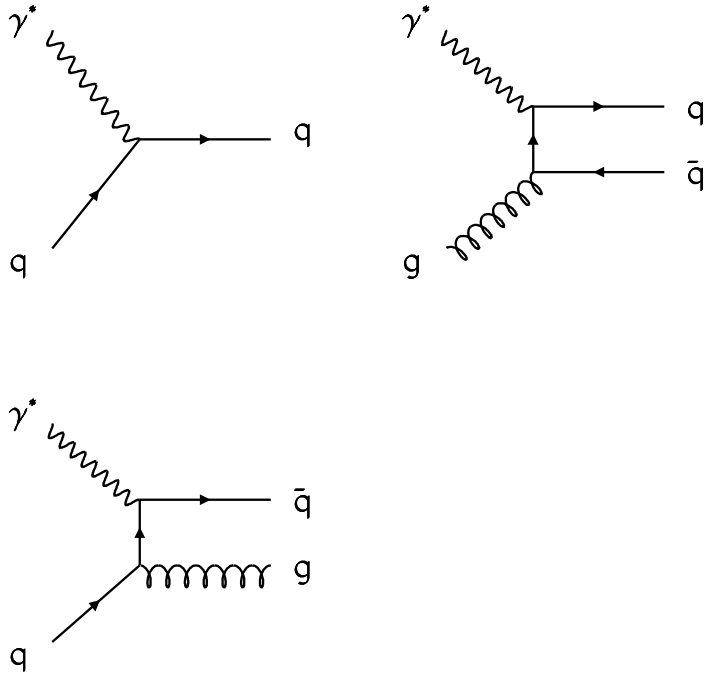

Figure 3.7: QCD Processes: Feynman graph for the process of the order α_{em} (QPM, "Born-Term") is shown as well as the diagrams of the order $\alpha_{em}\alpha_s$: Boson-Gluon-Fusion (BGF) and QCD-Compton Scattering (QCDC).

- Boson-Gluon-Fusion (BGF): The virtual photon annihilates with a gluon from the proton, whereby producing a quark-antiquark pair.

3.3.2 Kinematics of Diffractive Dijet Processes

Figure 3.8 illustrates an example of a Feynman diagram of diffractive deep-inelastic scattering responsible for dijet production. Square of the invariant mass of both hard partons is

$$M_{12}^2 = (q + \xi_p p)^2. \tag{3.9}$$

Here, ξ_p is the momentum fraction of the parton from the pomeron, which undergoes the scattering process, relative to the initial proton. It can be expressed as

$$\xi_p = x\left(1 + \frac{s_{12}}{Q^2}\right) \approx \frac{Q^2 + M_{12}^2}{Q^2 + W^2}. \tag{3.10}$$

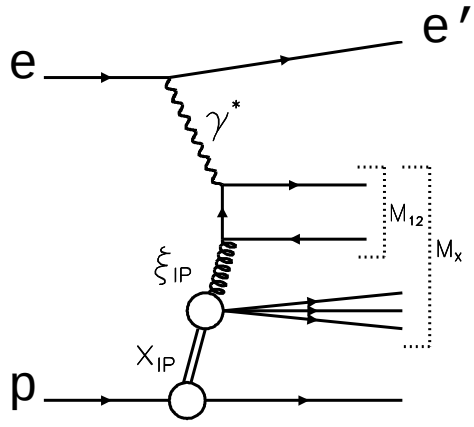

Figure 3.8: Kinematics of the diffractive dijet production: Above is depicted a Feynman graph of a QCD process of Boson-Gluon-Fusion of the photon with a gluon from the pomeron, which carries a momentum fraction $\xi_{I\!P}$.

As well the momentum fraction of the parton relative to the pomeron is no longer described by β. One has to introduce a new variable

$$\xi_{I\!P} = \frac{x}{x_{I\!P}} \left(1 + \frac{s_{12}}{Q^2}\right) \approx \frac{Q^2 + M_{12}^2}{Q^2 + M_X^2}. \tag{3.11}$$

$x_{I\!P}$, $\xi_{I\!P}$ and ξ_p are bound together by

$$\xi_p = x_{I\!P} \xi_{I\!P}. \tag{3.12}$$

3.4 Azimuthal Asymmetry of the Jet Plane

The most striking feature of the perturbative QCD calculation of diffractive $q\bar{q}$ final states is the ϕ^* dependence of jet production. Here ϕ^* is the angle between the lepton and the quark plane in the $\gamma^* p$ centre-of-mass system (see figure 3.9). Since it is difficult to identify the quark jet with the largest $p_\perp$ can be used.[1] The azimuthal asymmetry obtained after jet reconstruction is shown in figure 3.10, where also a comparison with the azimuthal asymmetry expected from a diffractive boson-gluon-fusion process with one gluon exchange (from a resolved pomeron) is given. Also at the hadron level the difference between the two approaches is clearly visible. [19]

The very specific signature of the perturbative QCD calculation becomes apparent only, when more detailed final state properties are considered. It

[1]The partons have the same $p_\perp$, but the reconstructed jets not necessarily because of the jet reconstruction.

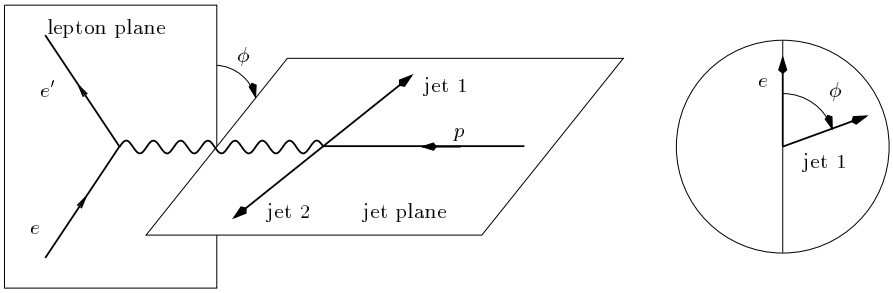

Figure 3.9: Definition of the azimuthal angle ϕ^* in the $\gamma^* p$ centre-of-mass system.

can be justified only for jets with large transverse momenta. This excludes any prediction for the diffractive structure function which may very well be dominated by pomeron-remnant jets. [22] In case of the high p_T dijet events the invariant mass of the dijet system M_{12} is identical to the total invariant mass of the diffractive system M_X. However depending on the jet algorithm used to identify the high p_T jets, a certain fraction of hadronic energy might not be associated to the jets. As well, one has to keep in mind that quite a large fraction of the $q\bar{q}g$ final states will appear as a two-jet configuration, and it will be difficult to separate them from the $q\bar{q}$ dijet final states. [20, 21]

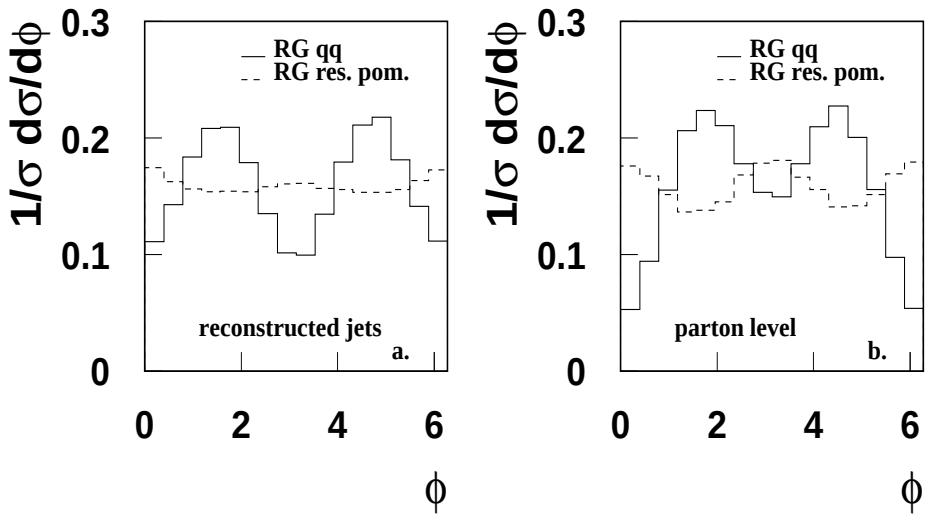

Figure 3.10: *(a)* The ϕ dependence of one jet with respect to the electron plane for high $p_\perp$ dijet events in the region $0.1 < y < 0.7$, $5 < Q^2 < 80$ GeV^2, $x_{I\!P} < 0.05$ and $p_\perp^{jet} > 2$ GeV. The solid line shows the prediction from the two gluon exchange mechanism after jet reconstruction at the hadron level. The dashed line shows the ϕ dependence from a BGF type process in diffraction (one gluon exchange). In *(b)* the ϕ dependence of the quark with respect to the electron plane is shown for comparison. The predictions are obtained with the RAPGAP Monte Carlo.

Chapter 4

The HERA Collider and the H1 Detector

At the DESY facility[1] in Hamburg, Germany, the unique lepton hadron collider HERA[2] is located. This chapter briefly introduces the collider and gives a basic description of the H1 detector and its components which are most important for this analysis.

4.1 The HERA Collider

HERA is the world's first and only electron-proton collider. The HERA collider consists of two separate storage rings in which the electrons[3] and protons are accelerated to their respective nominal collision energies and stored. The pre-accelerators PETRA, DESY II and DESY III provide electrons at an energy of 12 GeV and protons at an energy of 40 GeV which are then accelerated to their nominal energies of 27.5 GeV and 920 GeV respectively. The beams are brought into collision at two interaction points along the ring with a centre of mass energy of 319 GeV. The layout of the HERA accelerator is illustrated in figure 4.1.

4.2 Pre-Acceleration

Before being filled into HERA, the particles undergo several pre-acceleration steps. Electrons emerging from a LINAC[4] at energies of 450 MeV are accelerated up to 7.5 GeV in DESY II and then stored in PETRA II. After 60 electron bunches have been accumulated, they are accelerated to 12 GeV

[1] Deutsches Elektronen Synchrotron

[2] Hadron-Electron Ring Accelerator

[3] The term "electrons" will be used do denote both electrons and positrons throughout this thesis, unless otherwise specified.

[4] Linear Accelerator

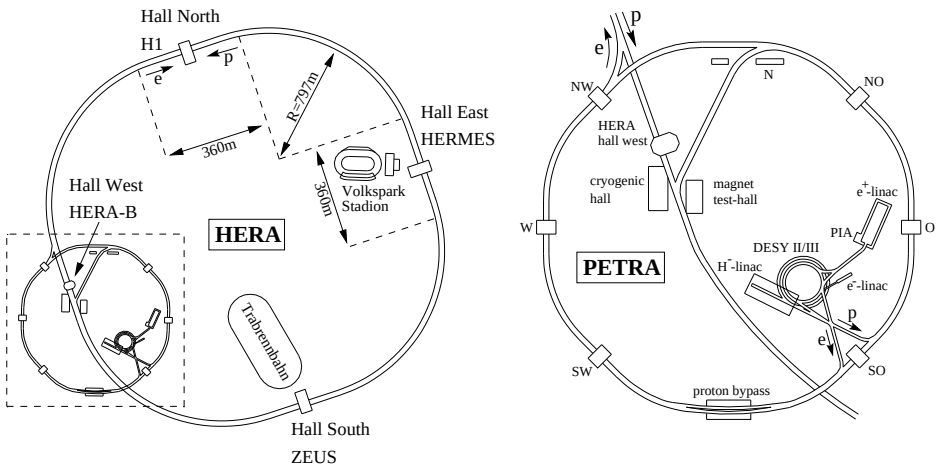

(a) (b)

Figure 4.1: The HERA collider *(a)* and its pre-accelerators *(b)*.

and injected to HERA-e. To produce free protons, negatively charged hydrogen ions of 50 MeV energy are shot onto a thin foil, which strips off the electrons. The remaining protons are accelerated to 7.5 GeV in DESY III and to 40 GeV in PETRA II before being injected into HERA-p.

4.3 The H1 Detector

A diagram of the central H1 detector is shown in figure 4.2. The detector has a mass of 2800 t and a size of $12\times10\times15$ m^3. The interaction point is located near the origin of the H1 coordinate system (small mark near 2). Electrons are entering from the left and protons come from the right. The positive z axis is defined by the direction of the incoming proton beam momentum. This direction is called the 'forward' direction. The coordinate x points to the centre of the accelerator ring, and y is pointing upwards. The polar scattering angle θ is measured with respect to the forward direction.

The general structure of the H1 detector follows the conventional design established for high energy particle physics experiments. The interaction region is surrounded by a tracking system which measures the transverse momenta of charged particles in magnetic field. The calorimeter is built around the tracking detector and measures energy depositions. Particles that are not stopped in the inner parts of the detector (mostly muons) are detected in the so-called central muon system. Because of the different beam energies of protons and electrons, the final state is not distributed symmet-

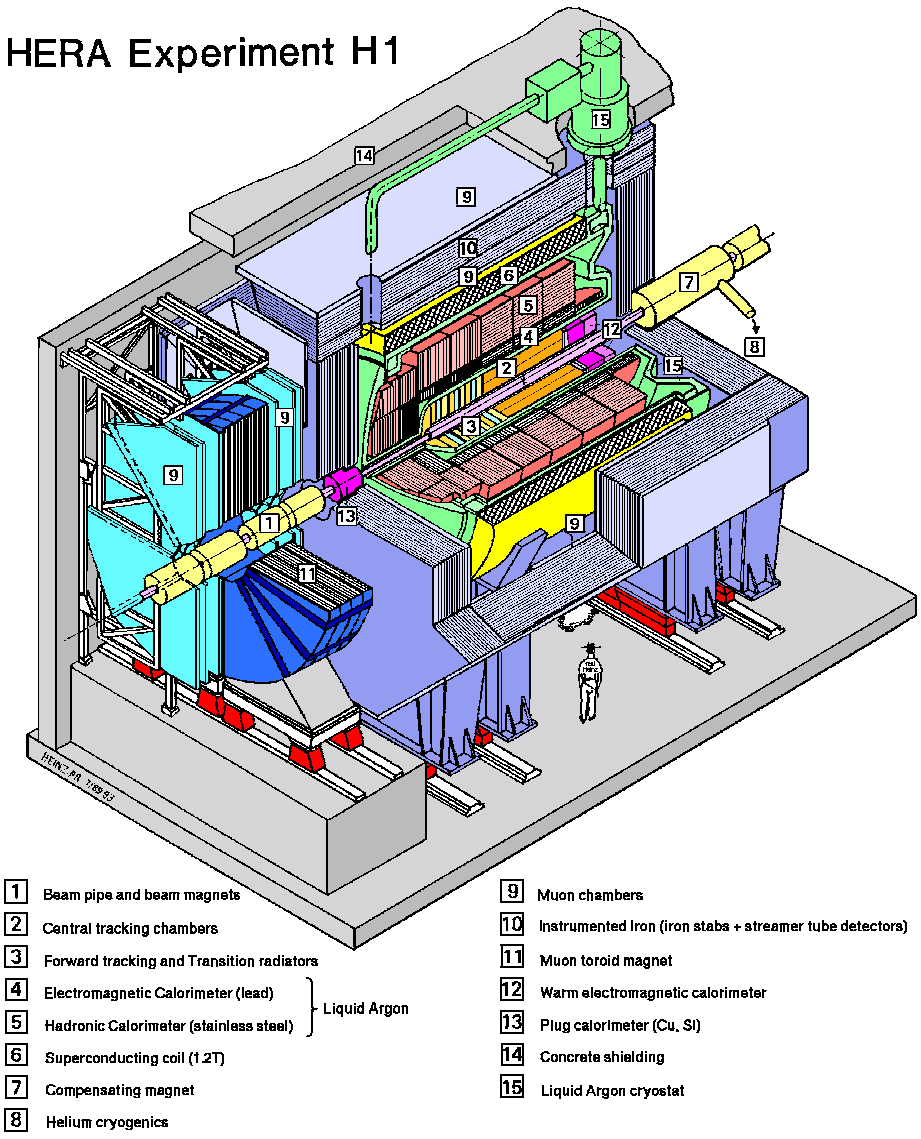

Figure 4.2: The H1 Detector.

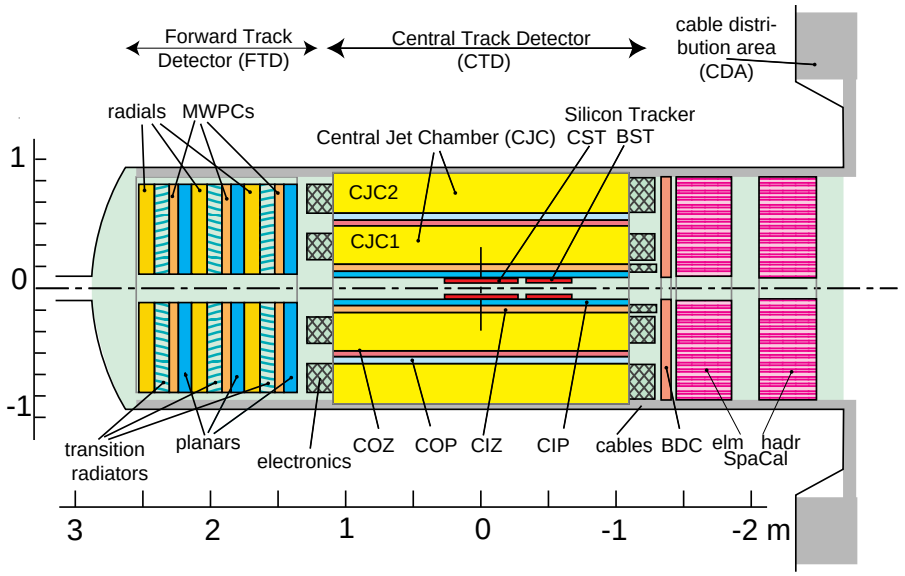

Figure 4.3: The tracking system of the H1 detector.

rically with respect to the interaction point. Instead it is boosted in the forward direction. The detector has a finer granularity in the forward region to obtain a better spacial resolution in that area. A complete description of the detector can be found in [1]. Here, only the components most relevant for the analysis are introduced.

4.3.1 Tracking detectors

A superconducting coil [6] produces a solenoidal magnetic field of strength 1.16 T parallel to the beam axis. Charged particles travelling in the perpendicular $x-y$ plane are subjected to the Lorentz force. The central tracking system [2] measures the particle trajectories. The transverse momentum and the electrical charge can be determined from the curvature of the trajectory. The tracking system is divided into a forward, a central, and a backward part. Only the central and backward tracking detectors are used in this analysis.

In the DIS analysis presented in this thesis, the backward drift chamber (BDC) is used to supplement the electron identification in the SPACAL calorimeter (figure 4.3).

4.3.2 Liquid argon calorimeter (LAr)

In the H1 experiment, the main calorimeter is a sandwich type calorimeter. It is composed of absorber plates and liquid argon as the active detection material. The argon is ionised by shower particles created in the absorber plates by the incident particle. The number of created ion-electron pairs is proportional to the energy of the incident particle. The electrons are collected on electrodes and a signal proportional to the electrical charge is read out. Because the ionisation process is of statistical nature, the absolute energy resolution is proportional to $1/\sqrt{E}$.

The LAr consists of an inner, electromagnetic part [4] with lead absorber plates corresponding to $20 \div 30$ radiation lengths with a relative energy resolution $\sigma_E/E = 11\%/\sqrt{E[\text{GeV}]}$ and an outer hadronic part [5] with stainless steel plates amounting to $4.5 \div 7$ interaction lengths with a relative resolution of $50\%/\sqrt{E[\text{GeV}]}$. The LAr is divided in z into eight self-supporting wheels; these are illustrated in figure 4.4(a). Each wheel is further divided in azimuthal angle ϕ into octants (figure 4.4(b)). The regions between wheels, and between octants, contain dead material; energy losses in these regions are difficult to control experimentally. The z-cracks and ϕ-cracks, which can be clearly seen as the whitespace in figure 4.4, are positioned to minimise the effect of energy leakage. The energy calibration has an uncertainty of 5%, which has to be added for both parts. The LAr covers the range $3.6 > \eta > -1.4$. The absolute hadronic energy scale is known within 4%.

4.3.3 Backward calorimeter SPACAL

The lead/scintillating fibre calorimeter SPACAL[5] [12] covers the backward range $-1.42 > \eta > -3.82$. Incident particles develop a shower in the lead which causes the fibres to scintillate. The light is detected in photomultiplier tubes. The calorimeter consists of an electromagnetic part with a depth of 28 radiation lengths and a hadronic part corresponding to 2 interaction lengths. Geometrical layout of the photomultiplier tubes in the electromagnetic part is depicted in the figure 4.5. The energy resolution in the electromagnetic part is $7\%/\sqrt{E[\text{GeV}]}$ [2]. An additional systematic uncertainty of 1% has to be added due to the electronics used to amplify the signals. The absolute electromagnetic energy scale is known to 0.3% for electron energies of 27.5 GeV and 2.0% for electron energies of 8 GeV. The absolute energy scale in the hadronic part of the SPACAL is known to 7%.

4.3.4 Forward detectors

The forward region is covered by the forward muon detector FMD and the proton remnant tagger PRT. The FMD consists of 6 double layers of drift

[5] 'spaghetti calorimeter'

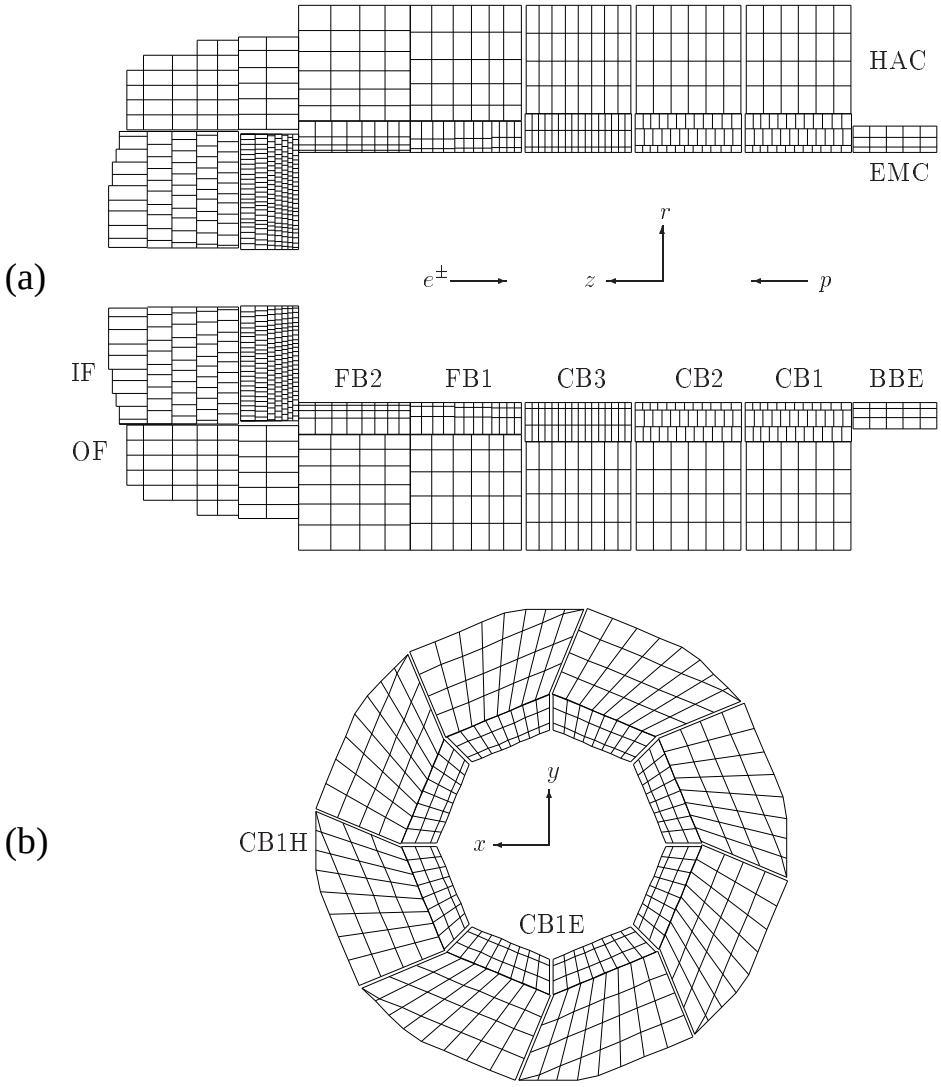

Figure 4.4: The cell structure of the LAr calorimeter: the wheel layout in the $r-z$ plane *(a)*, and the layout of wheel octants in the $r-\phi$ plane *(b)*.

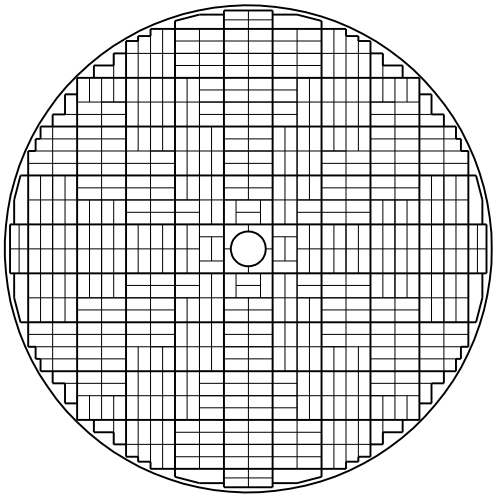

Figure 4.5: An $r - \phi$ sectional view of the electromagnetic part of the SPACAL calorimeter. The individual cells, each with their own photomultiplier, are joined together to form two-cell structures, show by thin lines. These are then combined into the 16 cell modules, the thick lines mark the borders, which are mounted around the beam-pipe.

chambers, four with wires perpendicular to the beam axis to measure θ and two with wires along the beam axis to measure ϕ. A charged particle produces a hit pair in a double layer. The FMD is placed outside of the massive iron yoke, having the main purpose of identifying muons from a collision event. However, it can also be reached by particles scattered by collimators around the beam pipe. The detector consists of 6 drift chambers [9], 3 of them being located behind a toroidal magnet [11]. The acceptance region is $2.9 > \eta > 1.4$ with a relative energy resolution of $24 \div 36\%$.

The PRT is located at $z = 26$ m in the HERA tunnel. It consists of seven scintillator layers which are shielded with lead. The detector can measure activity in the region $7 > \eta > 5.1$.

4.4 Data Acquisition and Trigger System

The probability for an interaction per bunch crossing is of the order of 10^{-3} [1]. Therefore, the rate of 10^7 bunch crossings per second translates into a collision frequency of 10^4 Hz, dominated by background processes. Physically relevant events are selected by a hardware trigger system. Signal patterns from various detector components are analysed to obtain a decision.

The trigger system is divided into five levels L1-L5. Based on triggers, L1 decides within 2 μs whether an event is rejected or kept. L1 is fully pipelined and therefore dead-time free. If at least one trigger is fired, the event is passed on to L2 for further examination. Typically, the L1 *keep signal* is sent at a rate of 50 Hz. For L2 the pipelines storing the full event information have to be stopped and read out. Based on correlations between the triggers, L2 gives a decision within 20 μs. If the event is not accepted by L2, the read-out is immediately stopped and data taking is continued, otherwise the event is fully read out. In the latter case, the total dead time is 1.5 ms. The event is directed to L4 (L3 is not yet operating) consisting of a parallel processor farm which operates a reduced version of the full reconstruction code. If it can verify the L1 and L2 keep signals, L4 stores the data on tape. The event is fully reconstructed off-line by L5.

Chapter 5

Kinematic Reconstruction

Having fixed centre of mass energy at HERA, the inclusive DIS processes can be described by two kinematic variables. The kinematics are over-constrained in NC events since there is redundant information from the measurement of both the lepton and the hadronic final state. There are then various methods available for the reconstruction of the kinematic variables. The choice of the method is based on several aspects, namely the acceptance of the detector, the influence of radiative corrections and the sensitivity to detector resolution. Each method has its kinematical range in which it can determine the variables with a better precision than the others. The methods of kinematic reconstruction useful for a DIS measurement are introduced in this section.

5.1 Electron Method

Using the energy E'_e and the angle θ_e of the scattered electron one obtains the kinematic variables as follows:

$$Q^2_e = 4E_e E'_e \cos^2 \frac{\theta_e}{2}, \tag{5.1}$$

$$y_e = 1 - \frac{E'_e}{E_e} \sin^2 \frac{\theta_e}{2}. \tag{5.2}$$

E_e in the latter equations stands for the energy of the initial electron.

The resolution of y_e degrades as y_e decreases whereas the resolution of Q^2_e remains good over the whole kinematic range.

5.2 Hadronic Method

The hadronic final state can be represented by the variables:

$$p_{T,h} = \sqrt{(\sum_i p_{x,i})^2 + (\sum_i p_{y,i})^2}, \tag{5.3}$$

$$\Sigma = \sum_i (E_i - p_{z,i}), \tag{5.4}$$

$$\tan\frac{\gamma_h}{2} = \frac{\Sigma}{p_{T,h}}. \tag{5.5}$$

The sums are over all particles in the hadronic final state. Using these the kinematic variables can be written as:

$$Q_h^2 = \frac{p_{T,h}^2}{1 - y_h}, \tag{5.6}$$

$$y_h = \frac{\Sigma}{2E_e}. \tag{5.7}$$

The hadronic reconstruction is used only for a Charged Current analysis, where the final state neutrino is not detected. For a Neutral Current measurement, the degrading Q_h^2 resolution with increasing y_h, and the comparatively large uncertainty in the hadronic measurement, makes it an undesirable method.

5.3 Double Angle Method

This method is based on mixture of the electron and hadron variables and uses measurements of two angles. One is the scattering angle θ_e of the outgoing electron, the other is the angle γ_h assigned to the hadronic final state:

$$\cos\gamma_h = \frac{p_{x,h}^2 + p_{y,h}^2 - (E_h - p_{z,h})^2}{p_{x,h}^2 + p_{y,h}^2 + (E_h - p_{z,h})^2}. \tag{5.8}$$

Then the kinematic variables are defined as:

$$Q_{DA}^2 = 4E_e^2 \left[\frac{\sin\gamma_h(1+\cos\theta_e)}{\sin\gamma_h + \sin\theta_e - \sin(\theta_e+\gamma_h)}\right], \tag{5.9}$$

$$y_{DA} = \left(\frac{E_e}{E_p}\right)\left[\frac{\sin\gamma_h + \sin\theta_e + \sin(\theta_e+\gamma_h)}{\sin\gamma_h + \sin\theta_e - \sin(\theta_e+\gamma_h)}\right], \tag{5.10}$$

where E_p is the energy of the initial proton.

Double angle method is, to a good approximation, insensitive to the calorimeter energy scale. It performs badly for small and large angles of the electron and the hadronic final state.

5.4 "y-weighted-averaging" Method

"y-weighted-averaging" method is derived from the variables calculated in the electron and the double angle method:

$$Q_y^2 = \frac{4E_e^2(1-y_y)}{\tan^2(\theta/2)}, \tag{5.11}$$

$$y_y = y_e^2 + y_{DA}(1 - y_{DA}). \tag{5.12}$$

It combines the good precision of the electron method at high y_e with the good precision of the double angle method at low y_{DA}.

5.5 Reconstruction of Hadronic Final State

For diffractive scattering events with a large rapidity gap, the hadronic final state, X, is fully contained within the detector. Thus its invariant mass, easily calculated as follows

$$M_X^2 = E_{had}^2 - p_{x,had}^2 - p_{y,had}^2 - p_{z,had}^2, \tag{5.13}$$

should be reconstructed with a good precision. There is also a way to gain the invariant mass associated with the "y-weighted-averaging" method:

$$M_{X,y}^2 = (E_{had}^2 - p_{x,had}^2 - p_{y,had}^2 - p_{z,had}^2)\frac{y_y}{y_h}. \tag{5.14}$$

Chapter 6

Event Selection

6.1 Offline Analysis and H1OO Software

The newest version of H1OO software[1] was used in order to carry out the offline analysis. This new software environment based on ROOT [26], written in C++ and utilising object oriented programming techniques, was designed and implemented over the course of the HERA luminosity upgrade project. The H1OO project has now reached a high level of maturity and exceeds the capabilities of the pre-exsisting H1 analysis software in many areas. A summary of the H1OO project can be found in [27].

6.2 Selection of DIS Events

Events triggered by the analysis sub-trigger form the basis of the event selection in data. Monte Carlo event sample is based on the choice of a suitable Monte Carlo generator. This section describes the cuts, in the selection of DIS events, which describe the DIS kinematic range, and which are laid on the electron candidate in the SPACAL, on the $\sum(E - p_z)$ of the final state and on the event vertex.

6.2.1 The DIS Kinematic Range

The DIS kinematic range of the measurement is confined to a region in which the geometric acceptance and reconstruction efficiency are high. The defined kinematic range in terms of Q^2 and y, for all the measurements in this thesis, is:

$$4 \text{ GeV}^2 < Q^2 < 80 \text{ GeV}^2, \tag{6.1}$$

$$0.05 < y < 0.70. \tag{6.2}$$

[1] release 2.8.15

The range in Q^2 is determined by the geometrical acceptance of the scattered electron in the SPACAL. The cut in the lower Q^2 region removes resolved photon photoproduction events that are not simulated in the Monte Carlo. For Q^2 values larger than around 100 GeV^2 the electron is scattered into the liquid argon calorimeter. Region of $y < 0.05$ is excluded from the data sample due to high beam-gas backgrounds. The upper limit in y is a result of the cut on the scattered electron energy.

6.2.2 The Electron Candidate

For events with $Q^2 \leq 100$ GeV^2 the SPACAL and BDC are used to identify the scattered electron. Proper measurement of the scattered electron is an input for the calculation of the kinematic variables Q^2 and y and for the Lorentz boost into $\gamma^* p$ centre of mass system. Two things have to be taken care of; accurate measurement of the energy E_e and the polar angle θ_e, and efficient rejection of misidentified electron candidates. These might be, for example, charged hadrons that in photoproduction events frequently go into the backward direction. Cuts applied to reject such candidates are explained in the following paragraphs.

The Energy of the Scattered Electron

The scattered electron showers in the electromagnetic part of the SPACAL. The resulting cluster, consisting of cells with energy depositions form the shower, is used to calculate the energy of the electron candidate. In case there are more scattered electron candidates within the SPACAL acceptance in an event, the one with the highest $p_\perp$ is selected. The scattered electron is accepted if the following conditions are fulfilled:

$$E_e > 8 \text{ GeV}, \qquad \theta_e < 178^\circ. \tag{6.3}$$

The threshold of 8 GeV has been chosen in order to remove almost all misidentified electron candidates. The angle $\theta = 178^\circ$ is the upper limit of the SPACAL acceptance.

The Energy in the VETO Layer

Furthermore, at small scattering angles of the electron (corresponding to low Q^2), leakage into the beam pipe has to be avoided to ensure a good energy measurement. For this purpose, the summed energy E_{veto} in the 4 cells of the *veto layer* of the SPACAL, directly adjacent to the beam pipe (see figure 6.1), is required to satisfy

$$E_{veto} < 1.0 \text{ GeV}. \tag{6.4}$$

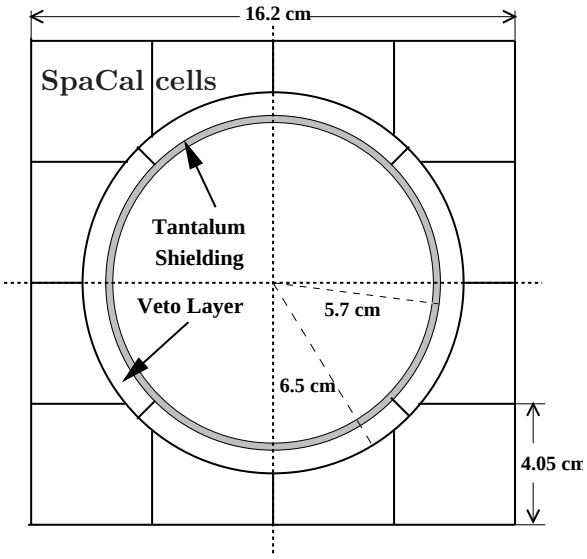

Figure 6.1: The (x, y) view of the SPACAL innermost cells and the VETO layer.

The Distance between SPACAL and BDC Extrapolation

The measurement of the electromagnetic cluster in SPACAL is complemented by tracking information provided by the BDC. Cluster from neutral hadrons, such as π^0, would not produce a track in the BDC. For this reason, the distance d_{BDC} between the SPACAL cluster centre of gravity and the closest track in the BDC should fulfil

$$d_{BDC} < 1.5 \text{ cm}. \tag{6.5}$$

The Energy in the Hadronic Part of the SPACAL

Because of the 28 radiation lengths of the electromagnetic part of SPACAL, showers of electrons with energies up to 27.5 GeV should be fully contained. Therefore, any activity in the hadronic section of the SPACAL behind the electron candidate is a sign of a hadron faking an electron. To quantify this, a variable E_{had} is defined by summing up the hadronic energy within a cone with 4° opening angle with respect to the direction of the electron candidate. E_{had} is required to satisfy

$$E_{had} < 0.5 \text{ GeV}. \tag{6.6}$$

The Radius of the Cluster in SPACAL

The radius of the cluster r_{cl} is required to satisfy

$$r_{cl} < 4 \text{ cm} \tag{6.7}$$

because the transverse dispersion within a calorimeter is larger for hadronic than for electromagnetic showers. The cut thus rejects photoproduction background.

The z-Position of the Cluster

The electromagnetic part of the SPACAL starts at $z = -150.5$ cm and the hadronic part at $z = -202$ cm. The active length of the electromagnetic part is 25 cm. A cluster that lies behind the electromagnetic part belongs rather to a hadron than to an electron. Therefore the scattered electron candidate has to pass the cut:

$$z_{clus} > -180 \text{ cm}. \tag{6.8}$$

The Radial Cluster Position in the SPACAL

A fiducial region is defined in the SPACAL in order to ensure a high quality selection of electron candidate with high efficiency. Due to high background levels, the innermost region of SPACAL is excluded by requiring the distance between the electromagnetic cluster and the beam pipe $d_{cluster-beampipe}$ to satisfy

$$d_{cluster-beampipe} > 9.1 \text{ cm}. \tag{6.9}$$

6.2.3 The $\sum(E - p_z)$ of the Final State

The $\sum(E-p_z)$ denotes the difference between the energy and z component of the momentum summed over all particles in the event. The $\sum(E-p_z)$ of the whole final state is calculated from a combination of track and calorimeter information, avoiding double counting. The value $\sum(E - p_z)$ is required to lie within the bounds

$$35 \text{ GeV} < \sum(E - p_z) < 70 \text{ GeV}. \tag{6.10}$$

The lower cut on the $\sum(E-p_z)$ of the final state reduces contamination from photoproduction events. In a fully contained event the value of $\sum(E - p_z)$ should be equal to twice the sum of the incident electron beam energy. In a photoproduction background event the final state electron disappears undetected into the backward beam-pipe and the $\sum(E - p_z)$ of the event is peaked towards lower values. The lower cut in $\sum(E - p_z)$ also reduces the contribution of events with significant bremsstrahlung radiation from the

initial state electron which affect the determination of the kinematical variables x, y and Q^2. The upper cut in $\sum(E-p_z)$ rejects poorly reconstructed events.

6.2.4 The Event Vertex

The rate of background from interactions between the proton beam and the residual molecules of gas in the beam-pipe, or with the walls of the beam-pipe upstream is high. Most of the resulting background events have a large number of tracks that do not point to a vertex near the nominal interaction point. To reduce this background the events are required to have a reconstructed vertex within 35 cm, along the z axis, of the nominal interaction point at $z = 0$, i.e. they satisfy the cut

$$|z_{vertex}| < 35 \text{ cm}. \tag{6.11}$$

6.3 Selection of Diffractive Events

The signature of a diffractive event is a 'rapidity gap' - a region of pseudorapidity between the proton-remnant system and the rest of the final state in which no hadrons are produced. In this analysis, the aim is to select diffractive events in which the proton is elastically scattered or forms only a low-mass state. In such events, the rapidity gap extends a long way in the forward direction - almost up to the proton beam direction. There are several detectors in this region, which are used to detect energy flow and thus veto non-diffractive or proton-dissociation events.

6.3.1 The Forward Detectors

The Liquid Argon Calorimeter (LAr)

The quantity η_{max} is defined as the pseudorapidity of the most forward calorimeter cluster of at least 400 MeV, this threshold being chosen as a compromise between efficiency and noise rejection. Clusters can be detected up to $\eta_{max} \approx 3.5$, at the forward edge of the LAr. The cut used is

$$\eta_{max} < 3.2. \tag{6.12}$$

The Proton-Remnant Tagger (PRT)

The PRT was designed specifically in order to veto proton-dissociation events by detecting particles in the very forward direction. If a hit is present in any of its five layers, the event is rejected.

$$\text{PRT}_{1,2,3,4,5} < 1 \tag{6.13}$$

The Forward Muon Detector (FMD)

The FMD is designed to detect and measure high-energy muons in the forward direction. However, it has also proved to be sensitive to particles from the proton remnant that scatter from the beam pipe and surrounding material. If more than one hit is detected in the first two layers of the FMD altogether, or if more than one hit is read in the third layer, then the event is rejected.

$$\mathrm{FMD}_{1+2} < 2, \qquad \mathrm{FMD}_3 < 2 \tag{6.14}$$

6.3.2 Cut on $x_{I\!P}$

The rapidity of the hadronic system X is largely dependent on the value of $x_{I\!P}$, so there is a strong correlation between $x_{I\!P}$ and η_{max}. The cut $\eta_{max} < 3.2$ restricts the accessible range of $x_{I\!P}$ to approximately $x_{I\!P} < 0.04$, hence a cut of

$$x_{I\!P} < 0.04 \tag{6.15}$$

is applied. The requirement of a small $x_{I\!P}$ and a clear rapidity gap ensures that the measurement covers the kinematic region where diffraction dominates, and any contribution from meson exchange is expected to be small.

6.4 Selection of Dijet Events

The observation of quarks as free particles is not possible due to its colour. The quarks produced in the hard interaction are fragmenting into hadrons which produced so-called jets of particles. These jets keep some of the kinematic characteristics of the corresponding quark or gluon, although they are quite smeared. The reconstruction of these jets of particles is done using *jet algorithms*. The resulting jets should be well correlated in momentum and angle with the quarks or gluons that produced them.

6.4.1 The k_T-Jet Algorithm

In this analysis the inclusive k_T-jet algorithm [18] is applied using the ΔR-resolution and the p_T-weighted recombination scheme. It is infrared and collinear safe and, neglecting particle masses, invariant under Lorentz boosts along the z-axis.

The algorithm successively combines objects, so-called protojets, when they are close to each other in pseudorapidity η and azimuthal angle ϕ. The distance in $\eta - \phi$ plane, ΔR, is weighted with their transverse momenta p_T such that low energetic objects are combined first. The algorithm starts with all input objects as protojets and ends with the jets using the following iterative technique:

1. For each protojet i and each pair of protojets ij the distances

$$d_i = p_{T,i}^2, \tag{6.16}$$

$$d_{ij} = min(p_{T,i}^2, p_{T,j}^2) \cdot [(\eta_i - \eta_j)^2 + (\phi_i - \phi_j)^2]/R_0^2 \tag{6.17}$$

   are calculated. R_0 is related to the opening angle of the jets and is set to $R_0 = 1$ in this analysis.

2. The minimum d_{min} of all d_i and d_{ij} is found.

3. If d_{min} is one of the d_{ij} the protojets i and j are replaced by a new protojet k with the merged kinematic quantities

$$p_{T,k} = p_{T,i} + p_{T,j}, \tag{6.18}$$

$$\eta_k = \frac{p_{T,i}\eta_i + p_{T,j}\eta_j}{p_{T,k}}, \tag{6.19}$$

$$\phi_k = \frac{p_{T,i}\phi_i + p_{T,j}\phi_j}{p_{T,k}}. \tag{6.20}$$

4. If d_{min} corresponds to one of the d_i then the protojet i is considered as a final jet and is removed from the list of protojets.

5. In case there are some protojets left the procedure continues on with the first step.

Particle masses are neglected in all steps leading to massless jets. The resulting jets are ordered according to decreasing p_T in the output list. Jets with transverse momentum smaller than a certain threshold $k_{T,min}$ are left out.

A short overview of different recombination and resolution schemes for the inclusive k_T-jet algorithm is given in [18].

6.4.2 Lorentz Boost into the $\gamma^* p$ Frame

The jet algorithm is applied after boosting the objects into the $\gamma^* p$ centre-of-mass frame defined by

$$q + p = l - l' + p = 0, \tag{6.21}$$

where l (l') is the 4-vector of the incoming (outgoing) electron, q (p) is the 4-vector of the exchanged photon (initial proton). The reason to go into this frame is that because the azimuthal asymmetry (see section 3.4) of the jet plane with respect to the lepton plane is exposed here. The other important aspect is the transverse momentum with respect to the photon-proton collision axis. The jet algorithm, hence also the cut on p_T of the jets, will be performed in this frame.

In order to see the azimuthal asymmetry one has to be sure that the boosting procedure works properly. A not properly defined system to boost to can result in producing unwanted azimuthal dependence. Thus the asymmetry can be correctly seen only in the $\gamma^* p$ centre-of-mass system. As an input to the boosting procedure the correct 4-vector l' of the scattered electron has to be given. Several methods of reconstructing the scattered electron characteristics are listed in chapter 5. These methods are then compared using the Monte Carlo information from the generator level, and the method that gives the best results is chosen.

Unwillingly a problem occurs when concerning the final state radiation. Photon radiated from the scattered electron is usually so close to the electron that these two particles are contained within the same clusters in the SPACAL, and thus cannot be distinguished separately. Events where the radiated gamma forms its own separate clusters in the calorimeter are rare. In such cases the measured scattered electron misses the energy and the momentum from the radiated photon, and its reconstructed 4-vector does not correspond to the 4-vector of the electron directly coming out of the lepton vertex. Thus the reconstructed 4-vector, that plays the crucial role in the definition of the $\gamma^* p$ centre-of-mass system, cannot be used as an input parameter for the boosting procedure. Not only the $\gamma^* p$ frame would be improperly defined, but the radiated gamma as a separate particle would figure as one of the input objects for the jet finder algorithm. Another case the reconstructed electron 4-vector misses the contribution of the radiated photon is the situation where the photon flies undetected into the beam-pipe.

By excluding those events, where there are more particles than the scattered electron in SPACAL, a majority of problematic events is excluded. Whole hadronic final state should thus be fully contained within the LAr calorimeter. That can be achieved by applying the following cut on pseudorapidity in laboratory frame of all the hadronic final state particles:

$$\eta_i > -1.5, \qquad i \in X. \tag{6.22}$$

Then, no angular dependence is produced by the wrong definition of the $\gamma^* p$ system due to ignoring the radiated photon 4-vector. And no high-energetic jets going in the direction of the scattered electron, and consisting mostly of one particle only (the radiated gamma) invade the set of jets formed by the hadronic final state.

6.4.3 Jet Selection

The parameters used to run the jet algorithm are

$$R_0 = 1, \qquad k_{T,min} = 3.5 \text{ GeV}. \tag{6.23}$$

Thus only the jets with the transverse momentum

$$p^*_{T,jet} > 3.5 \text{ GeV} \tag{6.24}$$

DIS kinematic range	$4\ \text{GeV}^2 < Q^2 < 80\ \text{GeV}^2$ $0.05 < y < 0.70.$
electron candidate	$E_e > 8$ GeV, $\theta_e < 178°$. $E_{veto} < 1.0$ GeV $d_{BDC} < 1.5$ cm $E_{had} < 0.5$ GeV $r_{cl} < 4$ cm $z_{clus} > -180$ cm $d_{cluster-beampipe} > 9.1$ cm
$\sum(E - p_z)$ of the final state event vertex	$35\ \text{GeV} < \sum(E - p_z) < 70\ \text{GeV}$ $\lvert z_{vertex}\rvert < 35$ cm
diffractive selection	$\eta_{max} < 3.2$ $\text{PRT}_{1,2,3,4,5} < 1$ $\text{FMD}_{1+2} < 2$, $\text{FMD}_3 < 2$ $x_{I\!P} < 0.04$
hadronic final state	$\eta_i > -1.5$, $i \in X$
jet selection	$p^*_{T,jet} > 3.5$ GeV $-3.0 < \eta^*_{jet} < 0.0$ $N_{jets} \geq 2$

Table 6.1: Summary of all analysis cuts.

are kept. The jets are required to lie within

$$-3.0 < \eta^*_{jet} < 0.0 \tag{6.25}$$

in the $\gamma^* p$ frame. This goes hand in hand with the cut on pseudorapidity of whole final state discussed in the previous paragraph. The events with at least two jets satisfying all these conditions are considered in this analysis:

$$N_{jets} \geq 2. \tag{6.26}$$

All the analysis cuts used for the event selection in the data as well as in the Monte Carlo samples are summarised in table 6.1.

Chapter 7

Data Selection

The data acquired in the years 1999 and 2000 were used in this analysis. Some of the features concerning the basic selection of the data will be outlined in this chapter.

7.1 General Event Selection

The event selection is based on a good *run* selection. A run is defined as the collection of a sequence of events over a time period with relatively stable beam, detector and trigger conditions. The run selection performed in this analysis takes into account the following factors that leads to a data sample with very good quality.

The first requirement of a good run is that the beam and the magnet parameters are stable and in the appropriate range. Secondly the High Voltage (HV) of CJC1 and CJC2 should be turned on, and the H1 detector status as well as the trigger system should be optimal for data taking.

A quality factor, so-called *run quality*, is attributed to every run. The levels of run quality are poor, medium, good and unknown. Only runs with medium or good quality are accepted. The quality is determined mainly online, taking into account the type and the number of operational detector components during the run time.

Another important factor is the position of the *primary vertex* in the z-direction. Due to the satellite bunches from the electron and proton beams, an unnegligible source of background overlap the ep events. In order to suppress these background events the z-vertex position is required to be less than 35 cm away from the nominal interaction point in both directions.

From the events passed so far, only the ones triggered by the subtrigger `S61` at L1 and L4 of the trigger system are selected. If the `S61` conditions are fulfilled, the event is stored.

7.2 Trigger Selection and Trigger Efficiency

In order to make maximum use of the available luminosity, in is necessary to choose a subtrigger that triggers on as much of the selected events as possible. This requires a high efficiency for the given event signature, and a low prescale value of the trigger.

For an analysis of jet production as presented in this thesis, a trigger which combines a trigger element based on an electromagnetic cluster in SPACAL (the electron candidate) in conjunction with a high p_T track signal in the central tracker (with a high efficiency for jet events) is optimal. The subtrigger `S61` embodies these properties.

7.2.1 Prescales

The chosen subtrigger have a prescale of 1 for most of the corresponding running periods. There is a small fraction of runs where the trigger used has a prescale greater than 1. In such cases the corresponding events are counted with a weight equal to the prescale. Runs where the prescale of the used subtrigger is greater than 15 are excluded from the analysis.

7.2.2 Trigger Efficiency

The efficiency of a given trigger for the selected sample of events can be determined by using an independent subtrigger which is called *monitoring trigger*. 'Independent' means that the studied trigger and the monitoring trigger have no trigger element in common. Subtrigger `S0`, based on SPACAL information only, is used as a monitor trigger to determine the trigger efficiency in this analysis.

The trigger efficiency is then given by

$$\epsilon_{trig} = \frac{N_{mon+trig}}{N_{mon}}, \tag{7.1}$$

where N_{mon} is the number of events where the monitor 'L1 actual' and 'L4 verified' trigger fired, and $N_{mon+trig}$ is the number of events where the monitor trigger fired as in the former case and the 'L1 raw' analysis trigger fired. As the data sample given by the analysis trigger is a subset of the sample where the monitoring trigger fired, the errors of the trigger efficiency are binomial.

The figure 7.1 shows the trigger efficiency as a functions of Q^2, transverse momentum of the jets, and azimuthal angle of the jets. The observed constancy of these functions is a sign of independence of the analysis trigger on the monitoring trigger. Thus the `S61` is a suitable trigger for this analysis.

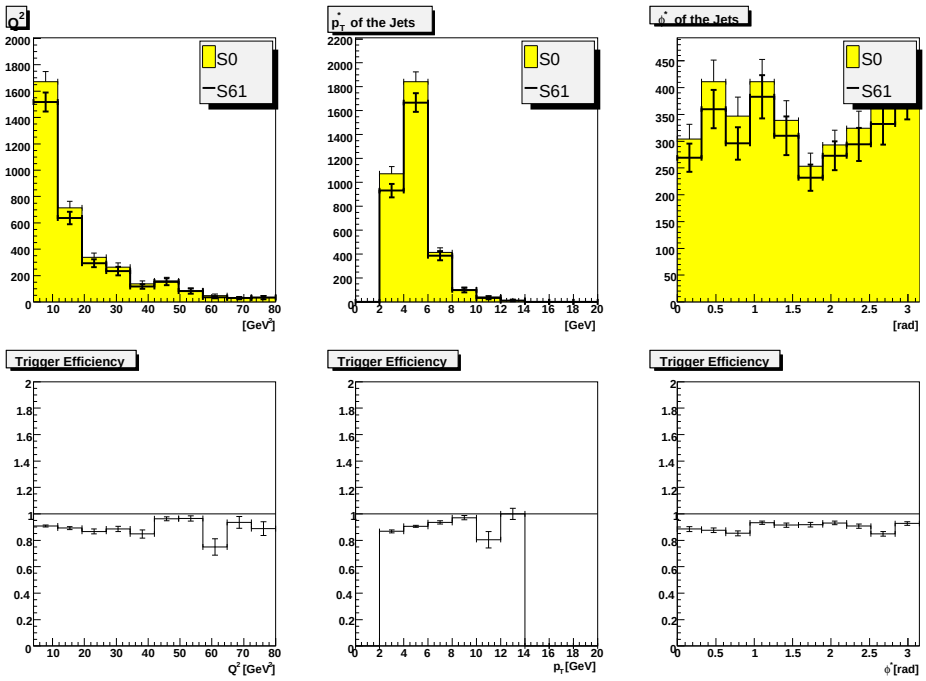

Figure 7.1: Trigger efficiency. The upper histograms show the distributions of Q^2, transverse momentum of the jets, and azimuthal angle of the jets. Each plot shows two distributions, one with the monitoring trigger fired and the other with the monitoring as well as the analysis trigger fired. The lower plots display just a fraction of the histograms above, i.e. show the trigger efficiency as a function of the relevant variables.

	99-00 data
kinematic and electron cuts	1892956
+ jet cuts	77894
+ diffractive cuts	3639

Table 7.1: Number of selected events after applying particular analysis cuts in the 99-00 data sample.

7.3 Data

The data sample selected so far is ready to undergo all the analysis cuts discussed in chapter 6. Decrease of number of events after applying particular cuts is shown in table 7.1. The final data sample consists of 3639 events only.

Chapter 8

Monte Carlo

In high energy physics Monte Carlo Event Generators are heavily used to compare experimental data with theoretical predictions. In experiments only stable particles are measured, but not partons (quarks and gluons), which cannot be described by perturbation theory, because the coupling constant α_s becomes large at scales of the order of the mass of hadrons. Thus the hadronisation has to be described by phenomenological procedures[1]. In Monte Carlo Event Generators one usually wants to calculate the cross section for various processes with the possibility to impose experimental cuts and to generate events according to theoretical distributions. These two subjects are closely related to each other.

A picture of our current understanding of the processes involved in high energy *ep* scattering (and its detection) is shown in figure 8.1. Different stages can be identified. First, final state partons are produced with certain 4-momenta. The kinematics and event quantities at the parton level are calculable within quantum field theory (supplemented by PDFs, which have to be extracted from measurements). Partons carry the colour quantum number. Colourless hadrons are formed in the process of fragmentation (also called hadronisation). Phenomenological models exist which describe this process. They have been tuned to describe existing measurements. The hadrons are measured in the detector. The finite resolution and geometrical acceptance of the apparatus will affect the measurement.

8.1 RAPGAP

RAPGAP is a Monte Carlo suited to describe deep inelastic scattering, including diffractive DIS and LO direct and resolved processes. [24]

The interpretation of the diffractive structure function F_2^D in terms of parton distribution functions, in analogy to the proton structure function,

[1]For example with the hadronisation packages JETSET or HERWIG.

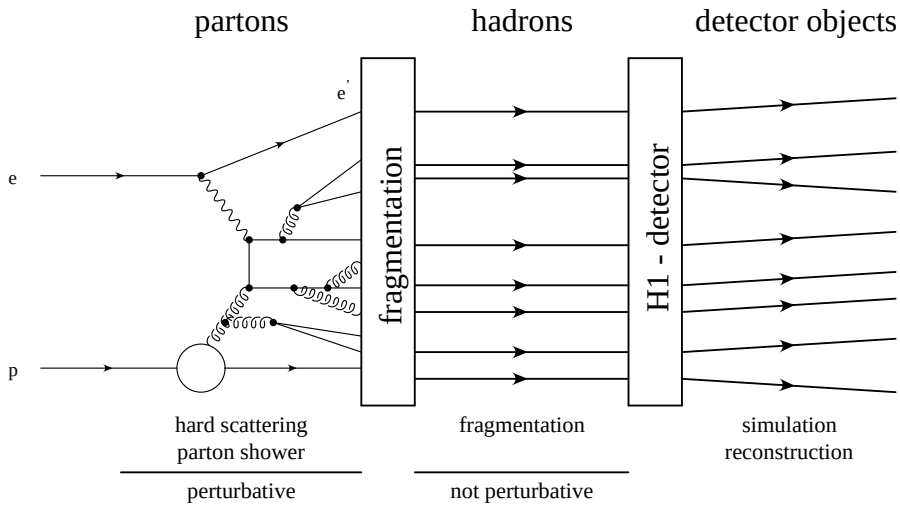

Figure 8.1: The picture of an ep collision and its detection as we currently understand it. The time evolves along the horizontal axis.

is not that clear and different approaches exist. Only the two relevant for this analysis are listed below.

- Resolved pomeron a la Ingelmann and Schlein: In the model of Ingelman and Schlein diffractive scattering is described in terms of pomeron $I\!P$ exchange, where the pomeron has a partonic structure.
- Two gloun exchange for diffraction: This approach is mainly intended to describe exclusive high p_T jet production. The perturbative calculation of $q\bar{q}$ and $q\bar{q}g$ final states can be used for light quark and heavy quark production. Due to the different gluon density parametrisations, different $x_{I\!P}$ dependencies of the cross section are expected. [19]

8.1.1 Resolved Pomeron

Resolved pomeron Monte Carlo generated using RAPGAP 2.08/18 for the purposes of the analysis of multiplicities in diffraction [25] is used here. It includes the quark-parton-model process of the order α_{em} and the two processes of the order $\alpha_{em}\alpha_s$, the boson-gluon-fusion and the QCD-Compton-scattering. This Monte Carlo consists of three sets of files. They are listed in table 8.1. As the sets do not contain same numbers of events, when putting them together one has to take care of assigning the right weights to each set. These weights are determined by the luminosity of the simulated processes. Contents of each set are listed in tables 8.2, 8.3 and 8.4. Figure 8.3 shows relative contribution of particular sets of files to the final event sample after

applying all the analysis cuts, and figure 8.2 shows the same event sample divided with respect to the processes it contains. Numbers of events in all sets after applying particular analysis cuts are summarised in table 8.5.

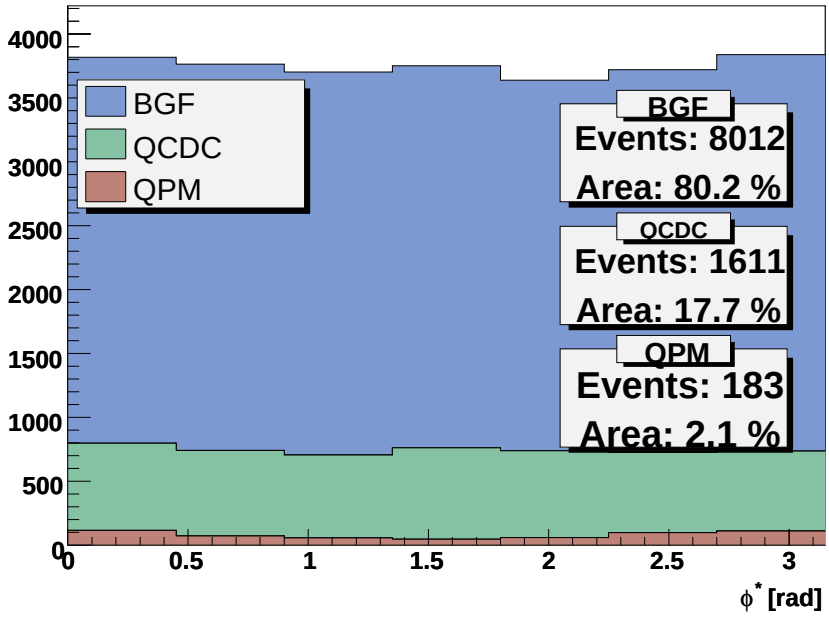

Figure 8.2: Relative contribution of particular processes contained in the resolved pomeron Monte Carlo after applying all analysis cuts. Histogram shows the azimuthal distribution of the jet plane in $\gamma^* p$ centre-of-mass system.

8.1.2 Two Gluon Exchange

There were no Monte Carlo files available with the two gluon exchange simulated. Using the newest version of RAPGAP available (version 3.1) two sets of files were generated, one with the $q\bar{q}g$ process and the other with the $q\bar{q}$ process[2]. Number of generated events together with a luminosity for each set are listed in the table 8.6. Cross sections of both considered processes are written in the table 8.7. Again, when putting the sets together, events from both sets have to be weighted according to the luminosity. Relative contribution of these sets containing one process each is shown in figure 8.4.

[2]The RAPGAP parameter `IPRO` is set to 20, 21 for the $q\bar{q}g$ and $q\bar{q}$ processes, respectively.

	Number of Generated Events	Luminosity
set 1	5000000	205 pb^{-1}
set 2	500000	179 pb^{-1}
set 3	4489194	95 pb^{-1}

Table 8.1: Resolved pomeron Monte Carlo: Sets of files.

Subprocess	Cross Section
QPM	33108 pb
BGF (light quarks)	922 pb
QCDC	380 pb

Table 8.2: List of processes in the set 1 of the resolved pomeron Monte Carlo.

Subprocess	Cross Section
QPM	5 pb
BGF (charm)	3687 pb

Table 8.3: List of processes in the set 2 of the resolved pomeron Monte Carlo.

Subprocess	Cross Section
QPM	57568 pb
BGF (light quarks)	1076 pb
BGF (charm)	3990 pb
QCDC	380 pb

Table 8.4: List of processes in the set 3 of the resolved pomeron Monte Carlo.

	set 1	set 2	set 3	total
	5000000	500000	4489094	9989094
kinematic and electron cuts	2463718	309898	2215177	4988793
+ jet cuts	18016	9999	15385	43400
+ diffractive cuts	5724	3143	939	9807

Table 8.5: Number of selected events after applying particular analysis cuts in resolved pomeron Monte Carlo.

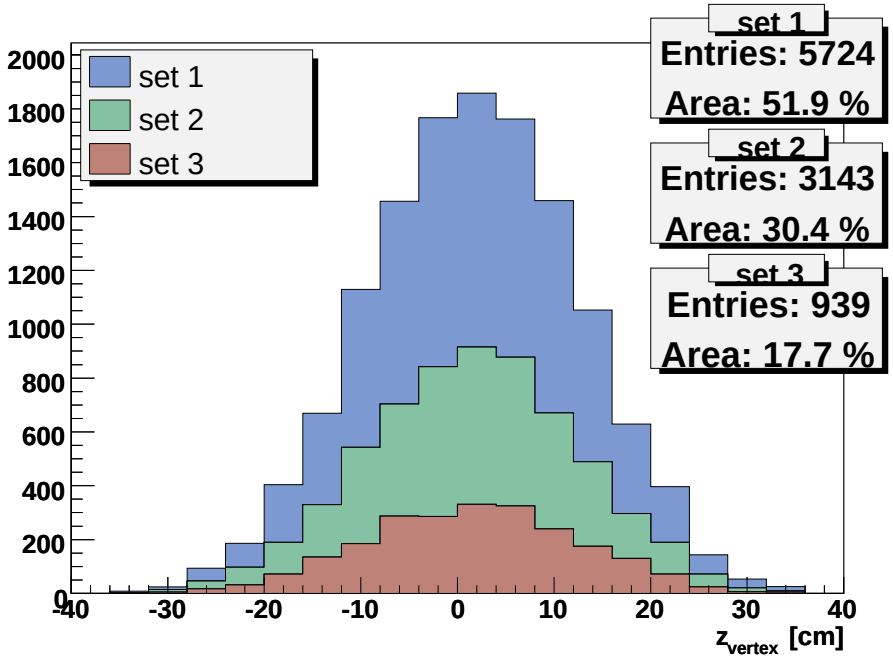

Figure 8.3: Relative contribution of particular sets of files contained in the resolved pomeron Monte Carlo after applying all analysis cuts. Histogram shows the distribution of the z coordinate of the primary vertex.

It displays only those events that fulfil all the analysis cuts. Numbers of events in both sets after applying particular cuts are summarised in table 8.8.

As already mentioned, the choice of the unintegrated gluon density affects the dependence of the cross section on $x_{I\!P}$. All files were generated using the derivative GRV[3].

	Number of Generated Events	Luminosity
$q\bar{q}g$	2500002	3037 pb^{-1}
$q\bar{q}$	5000002	30591 pb^{-1}

Table 8.6: Two gluon exchange Monte Carlo: Sets of files.

[3]Unintegrated gluon densities are selected via the parameter `IGLU` in RAPGAP. Derivative GRV corresponds to `IGLU` = 2.

Subprocess	Cross Section
$q\bar{q}g$	832 pb
$q\bar{q}$	165 pb

Table 8.7: Cross Sections of the processes in the two gluon exchange Monte Carlo.

	$q\bar{q}g$	$q\bar{q}$	total
	2500002	5000002	7500004
kinematic and electron cuts	1763898	3338124	5102022
+ jet cuts	73531	8492	82023
+ diffractive cuts	54145	6541	60686

Table 8.8: Number of selected events after applying particular analysis cuts in two gluon exchange Monte Carlo.

8.2 Reconstruction of Generated Variables

The correction for detector smearing is determined using generated Monte Carlo events for which the full detector response has been simulated. A Monte Carlo generator event output consists of a list of particles with certain quantum numbers and their 4-vectors. To obtain the detector response to the event, the interactions of the particles with the detector material must be evaluated. For H1 detector, the program H1SIM based on the GEANT package performs these calculations. Each particle is treated individually in its passage through the detector. The probability for a particle to interact with the detector material is evaluated using tabulated cross sections. These interactions may result in secondary particles, which themselves must be traced. Finally the detector response is obtained in the form of simulated electronic signals. These signals are then subjected to the same analysis chain as the signals from real particle collisions.

8.2.1 Reconstruction of Kinematic Variables

Chapter 5 lists several methods of reconstruction of generated kinematic variables. This paragraph concentrates on selecting the method that appears to be the most convenient to use in this analysis, i.e. gives the best agreement between generated and reconstructed values. The process of simulation of the detector response results in slight smearing of the original particle properties. It corresponds with the real passage of the particles through the detector and reflects the statistical nature of particle interactions.

When comparing different methods one looks how well are the same variables correlated at the generated and the reconstructed level. To have a clear illustration of how the procedure of reconstruction works along the whole

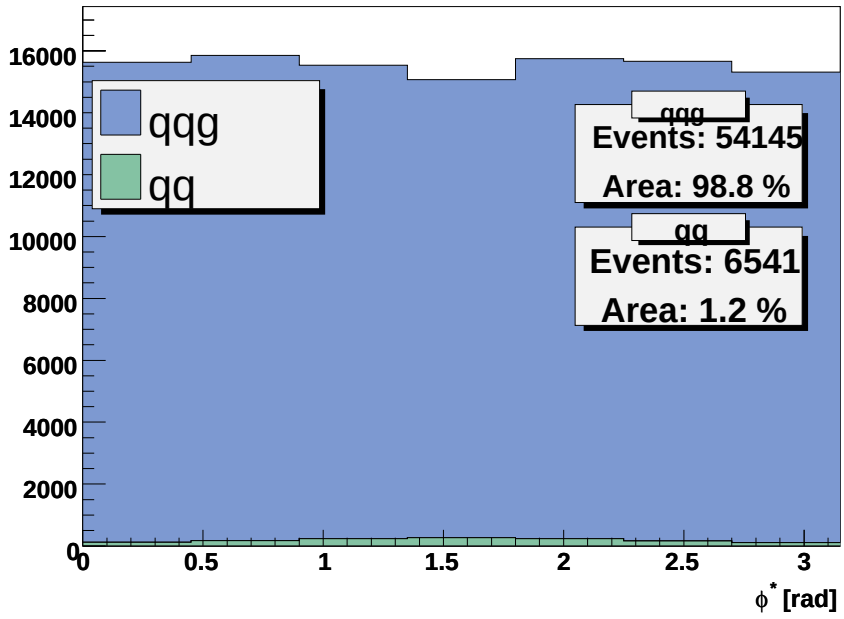

Figure 8.4: Relative contribution of particular processes contained in the two gluon exchange Monte Carlo after applying all analysis cuts. Histogram shows the azimuthal distribution of the jet plane in $\gamma^* p$ centre-of-mass system.

range of generated values it is useful to plot the reconstructed values as a function of the generated. To decide in behalf of one particular method one usually plots the so-called *resolution*, a histogram of $\frac{gen-rec}{gen}$. The resolution histogram points at two things. Its mean value tells whether the reconstruction process gives on average the same values as were generated or whether they are somehow shifted. And the width of the resolution peak refers to the precision of the reconstruction. The narrower the peak is, the smaller the effect of smearing of generated values is. It is the latter criterium, the width of the peak, that plays the leading part in choosing the right method.

All the methods discussed in chapter 5 were investigated on basis of its resolution histogram. Figures 8.5 and 8.6 illustrate just the electron and "y-weighted-averaging" method applied on the resolved pomeron Monte Carlo, respectively. Other methods mentioned in chapter 5 give worse results. On grounds of resolution the electron method has been chosen as the best. Same arguments point in favour of the electron method in case of the two gluon exchange Monte Carlo.

As the aim of this analysis is to study dijet events, it is worth looking at

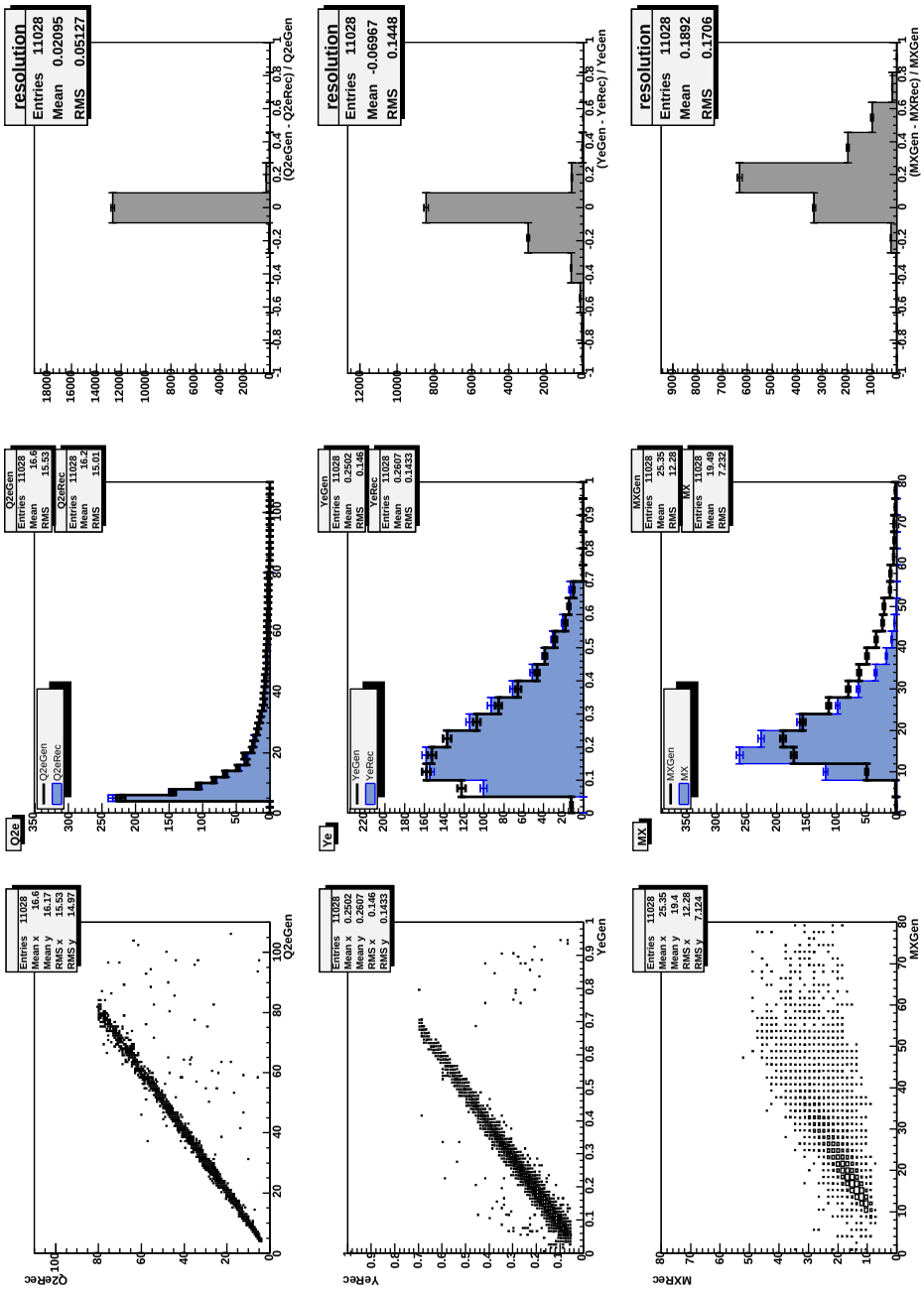

Figure 8.5: Reconstruction of kinematic variables Q^2, y and the hadronic final state mass M_X using the electron method in the resolved pomeron Monte Carlo.

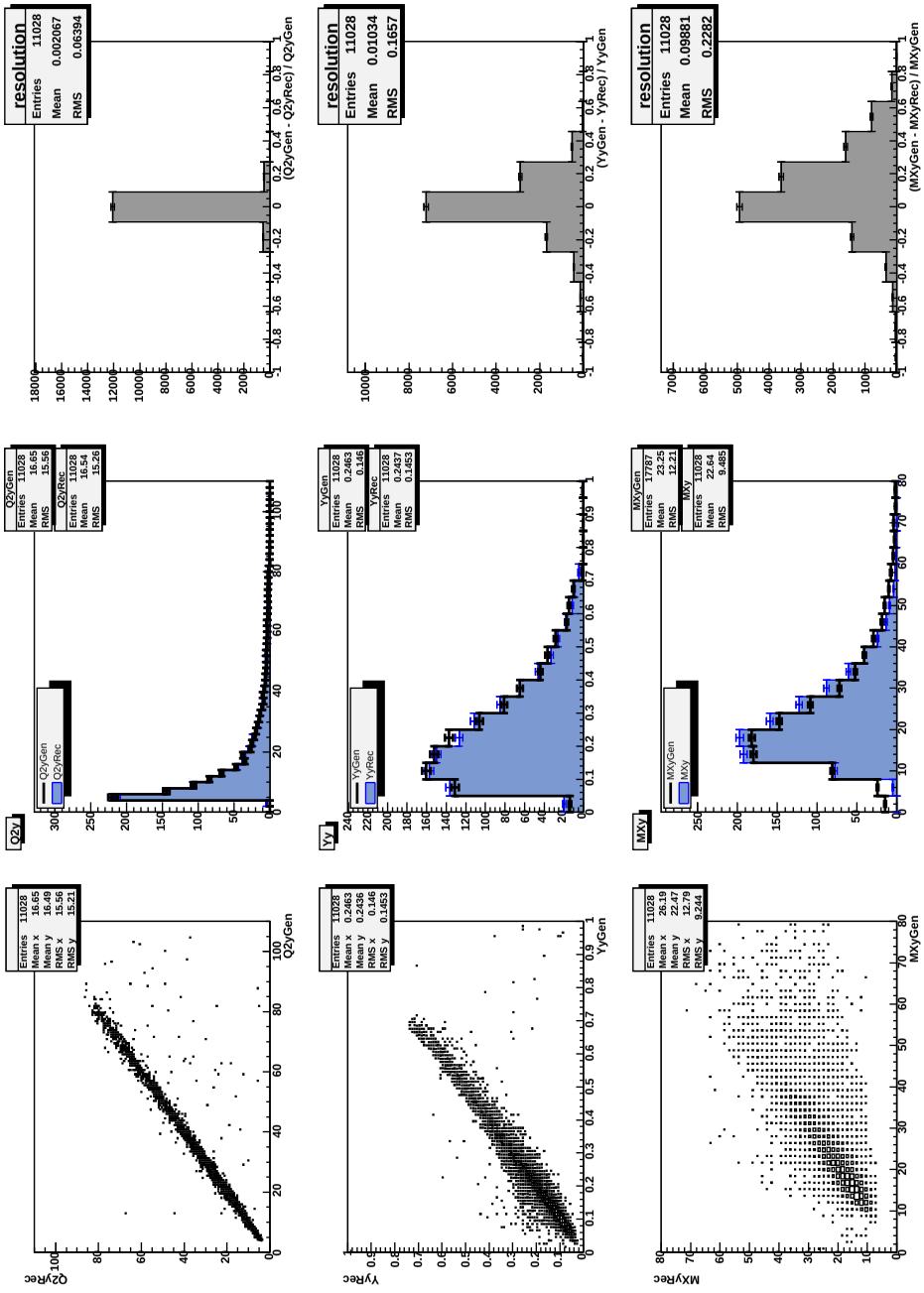

Figure 8.6: Reconstruction of kinematic variables Q^2, y and the hadronic final state mass M_X using the "y-weighted-averaging" method in the resolved pomeron Monte Carlo.

the reconstruction of dijet kinematics. Kinematic variables β, $\xi_{I\!P}$ are derived from the basic quantities Q^2, M_X and M_{12}. Thus it is not a reconstruction in the same sense as was discussed in the previous paragraph. Figures 8.7 and 8.8 just show how does the reconstruction of the basic quantities using different methods affect the quantities derived from them. Dijet kinematic variables play a crucial role in determining kinematic regions where the azimuthal asymmetry of the dijet plane is apparent. Again, the electron method gives better results on grounds of the resolution. Both β and $\xi_{I\!P}$ at the generator level are not well reproduced at the reconstructed level. Unfortunately, the region of $\xi_{I\!P}$ close to 1, where the smearing results in nearly zero statistics of events remaining in there, turns out to be the most convenient to point out the azimuthal asymmetry predicted by the two gluon exchange model. (see chapter 10)

8.2.2 Parton-Jet Correlation

Quarks cannot be directly measured in the experiment and are seen in form of jets after a hadronisation process. It is necessary to check whether the observable characteristics of these jets are related to the parton properties.

To study the correlations, first of all the two jets reconstructed via the jet algorithm have to be matched with corresponding two partons at the generator level. The assignment of partons to jets is done by means of the following procedure. The distance $R_{jet-parton}$ in the $\eta^* - \phi^*$ plane, defined as

$$R_{jet-parton} = \sqrt{(\Delta\eta^*)^2 + (\Delta\phi^*)^2}, \tag{8.1}$$

is calculated for every jet-parton pair. The jets are bound with those partons that give the minimal value of the sum $R_{jet_1-parton_1} + R_{jet_2-parton_2}$.

Parton-jet correlations are studied only for those events that fulfil all the analysis cuts at the detector level. At the parton level there are no kinematic requirements. In case of the two-gluon-exchange model both processes are taken into account. In case of the resolved pomeron Monte Carlo the correlations are done only for boson-gluon-fusion and QCD-Compton processes.

As seen in the figure 8.2 the bare quark parton model process does not have a significant influence on the dijet production. Moreover it lacks sense to correlate two jets with a single parton coming out of the hard interaction and the pomeron remnant, since no specific azimuthal dependence is awaited here.

Figures 8.9 and 8.10 show the correlations of partons and reconstructed jets in the resolved pomeron Monte Carlo. Figures 8.11 and 8.12 show the same correlations in the two gluon exchange Monte Carlo. As displayed in these figures, the reconstructed jets do keep the direction laid down by the partons. The correlations in transverse momenta are much worse. That is mainly caused by the parton showers and hadronisation. The harder jet

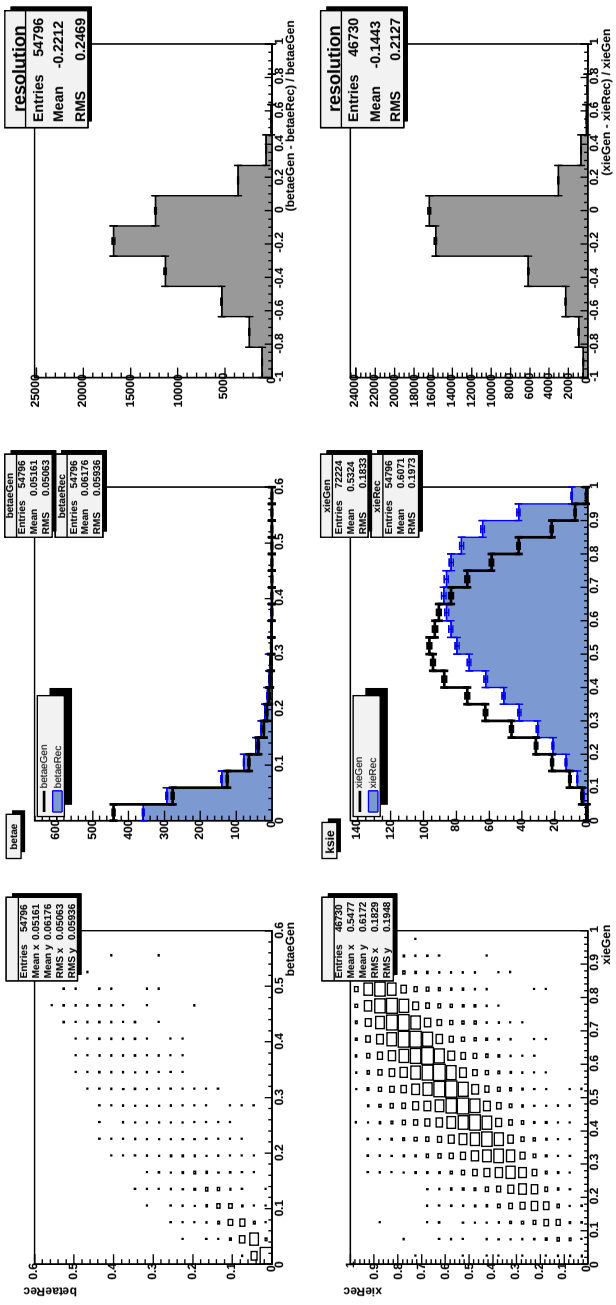

Figure 8.7: Reconstruction of dijet kinematic variables β and $\xi_{I\!P}$ using the electron method in the two gluon exchange Monte Carlo

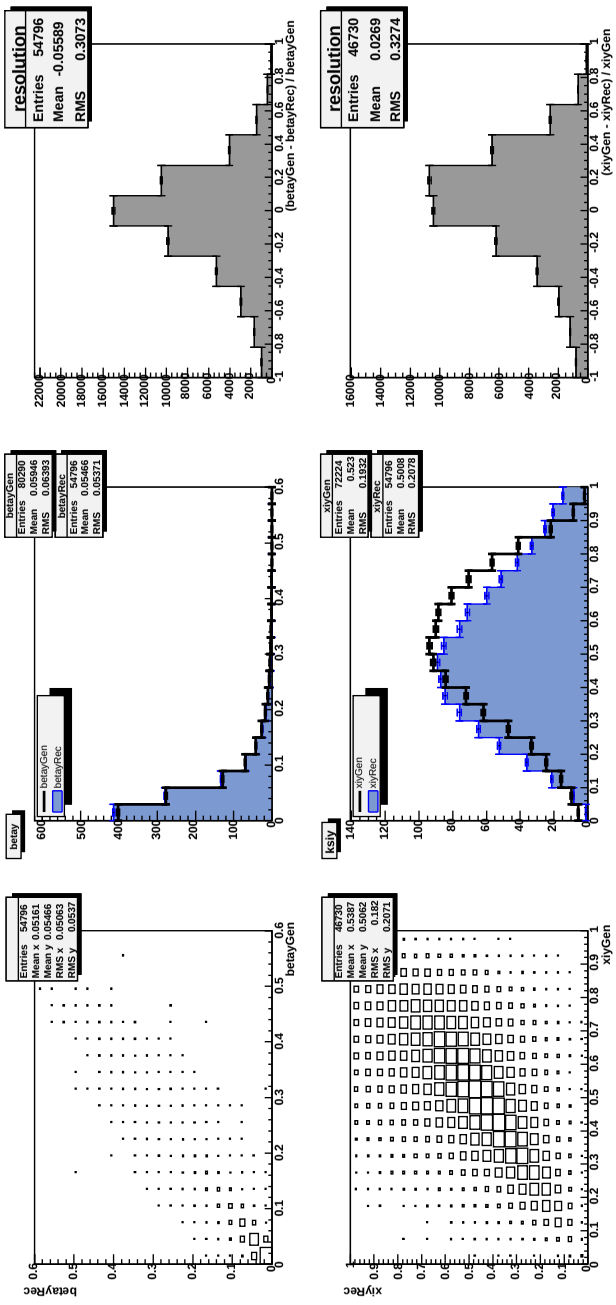

Figure 8.8: Reconstruction of dijet kinematic variables β and $\xi_{I\!P}$ using the "y-weighted-averaging" method in the two gluon exchange Monte Carlo

observed is not always coupled with the harder parton. The small peak seen in the p_T distributions of partons matched with the jets in case of the two gluon exchange model reflects the presence of the third parton (in $q\bar{q}g$ process) that contributes to the jet p_T as well.

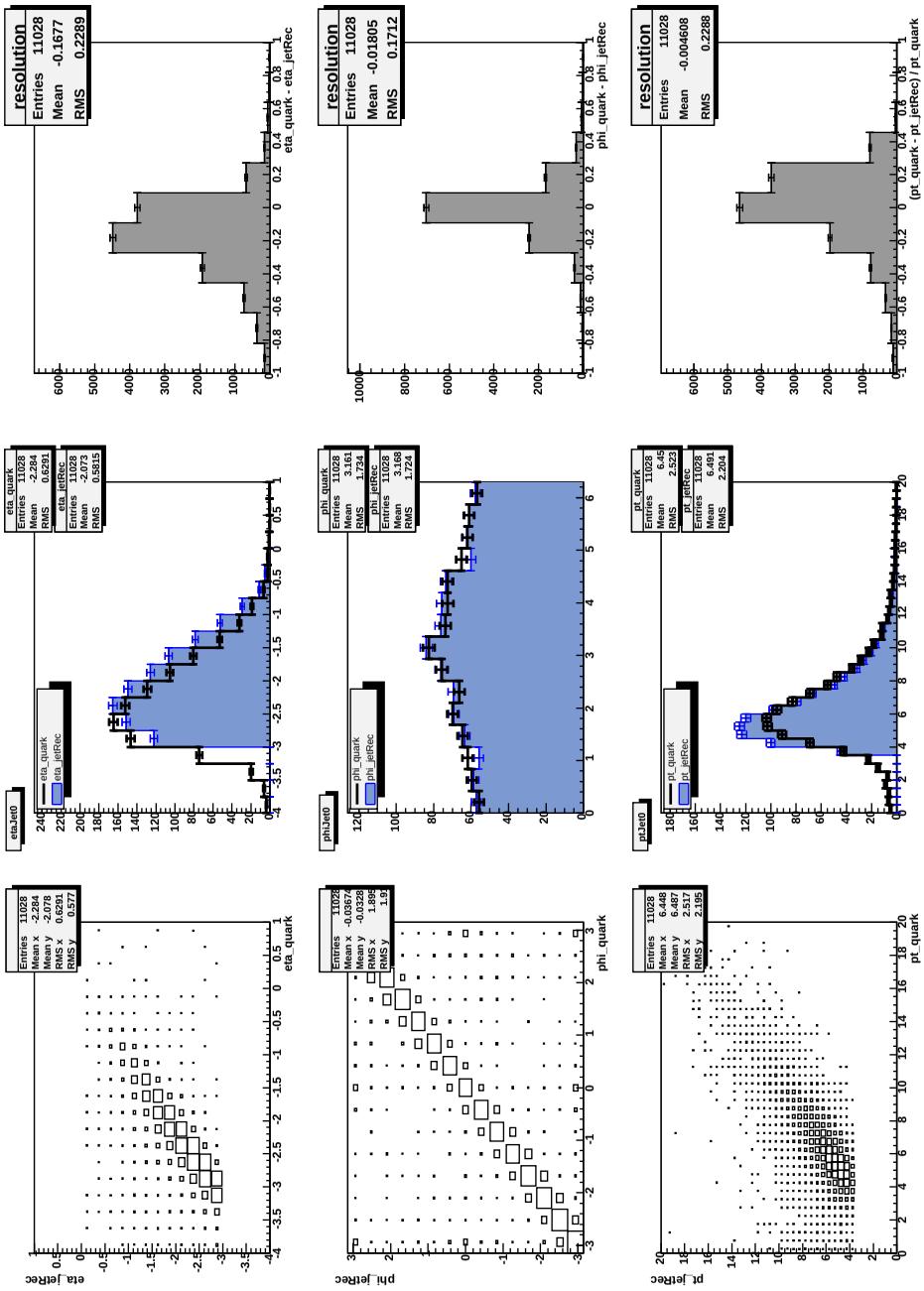

Figure 8.9: Correlation in η^*, ϕ^* and $p_\perp^*$ of the jet with the higher $p_\perp^*$ at the reconstructed level with the corresponding parton in the resolved pomeron Monte Carlo.

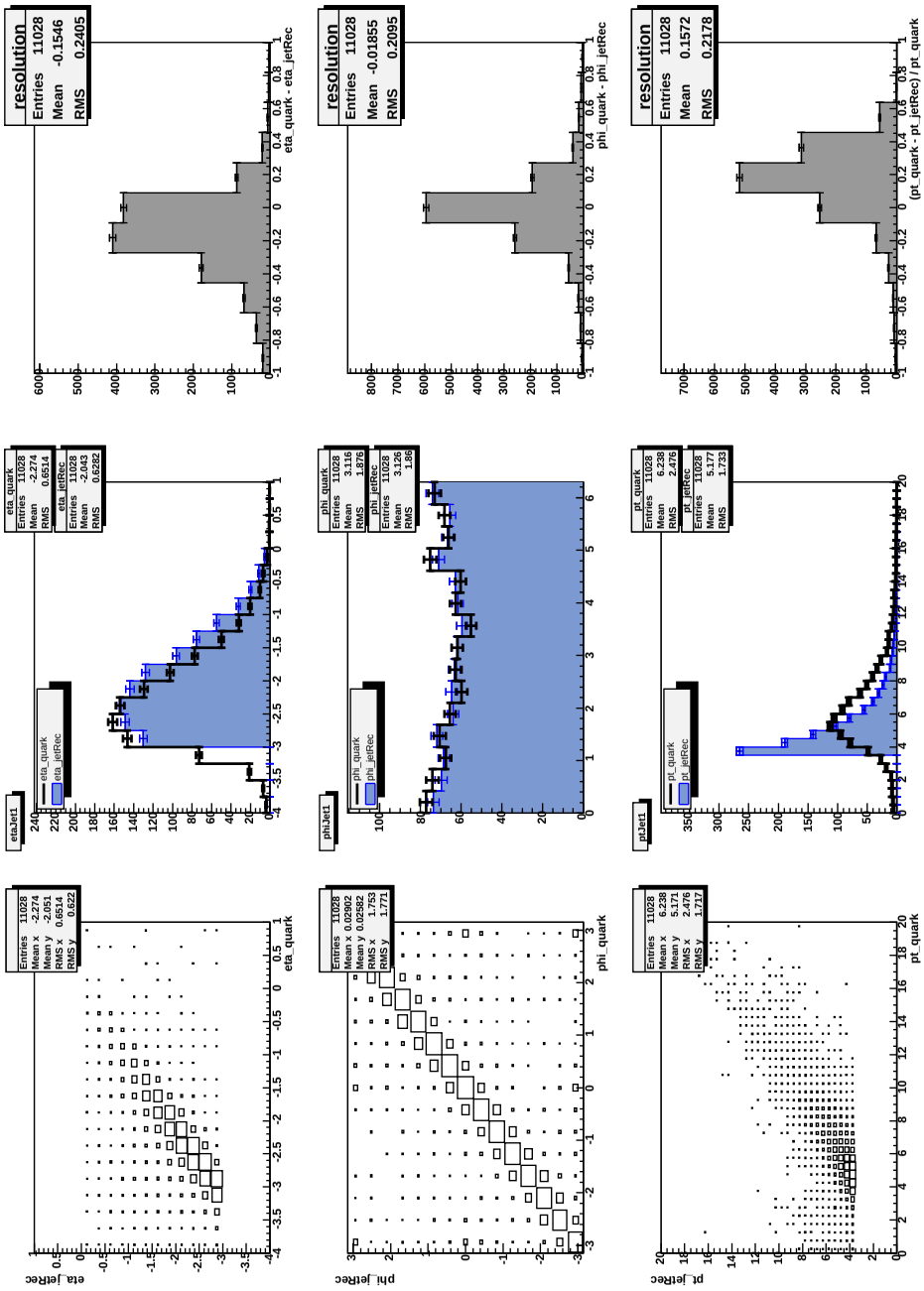

Figure 8.10: Correlation in η^*, ϕ^* and $p_\perp^*$ of the jet with the lower $p_\perp^*$ at the reconstructed level with the corresponding parton in the resolved pomeron Monte Carlo.

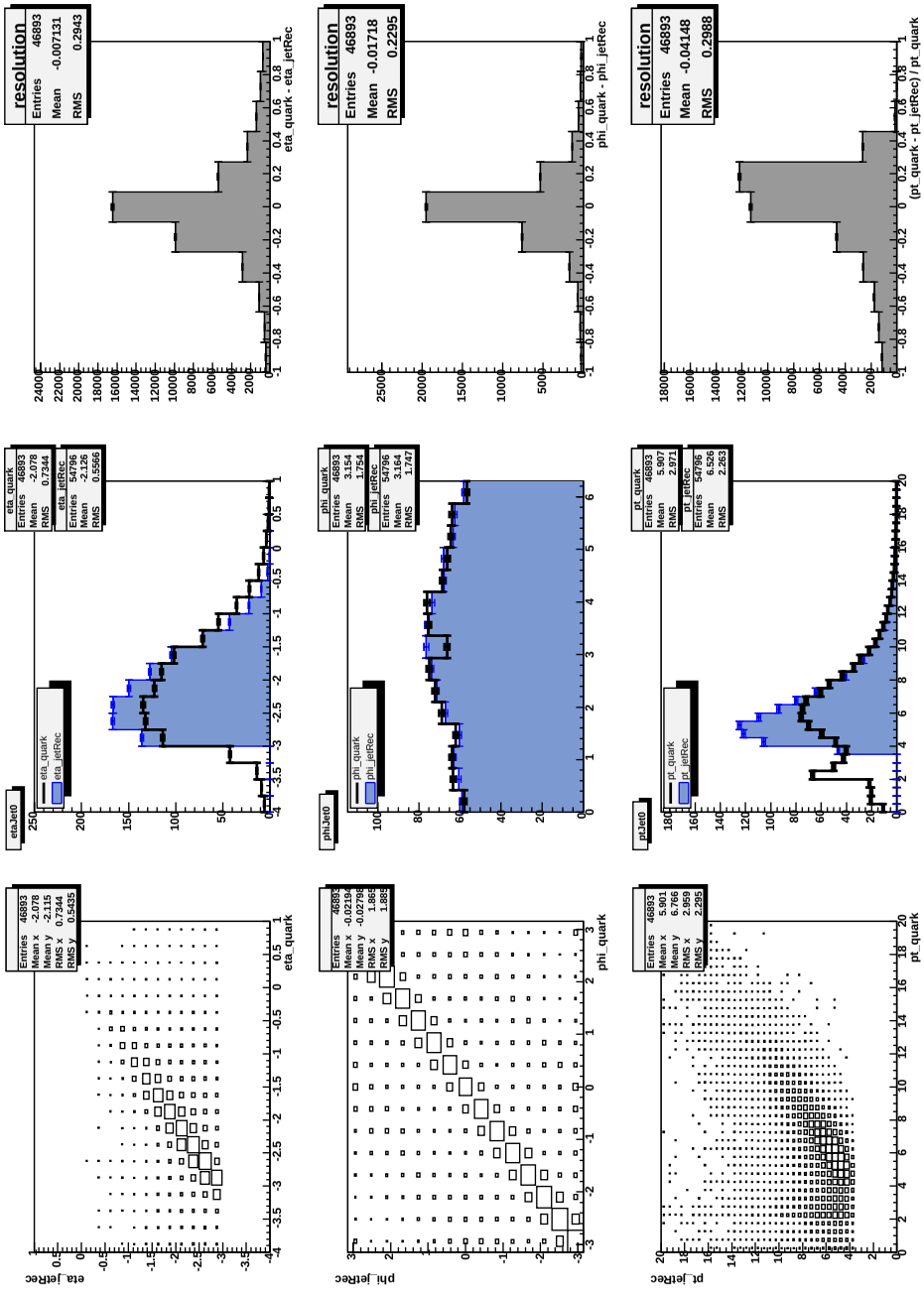

Figure 8.11: Correlation in η^*, ϕ^* and $p_\perp^*$ of the jet with the higher $p_\perp^*$ at the reconstructed level with the corresponding parton in the two gluon exchange Monte Carlo.

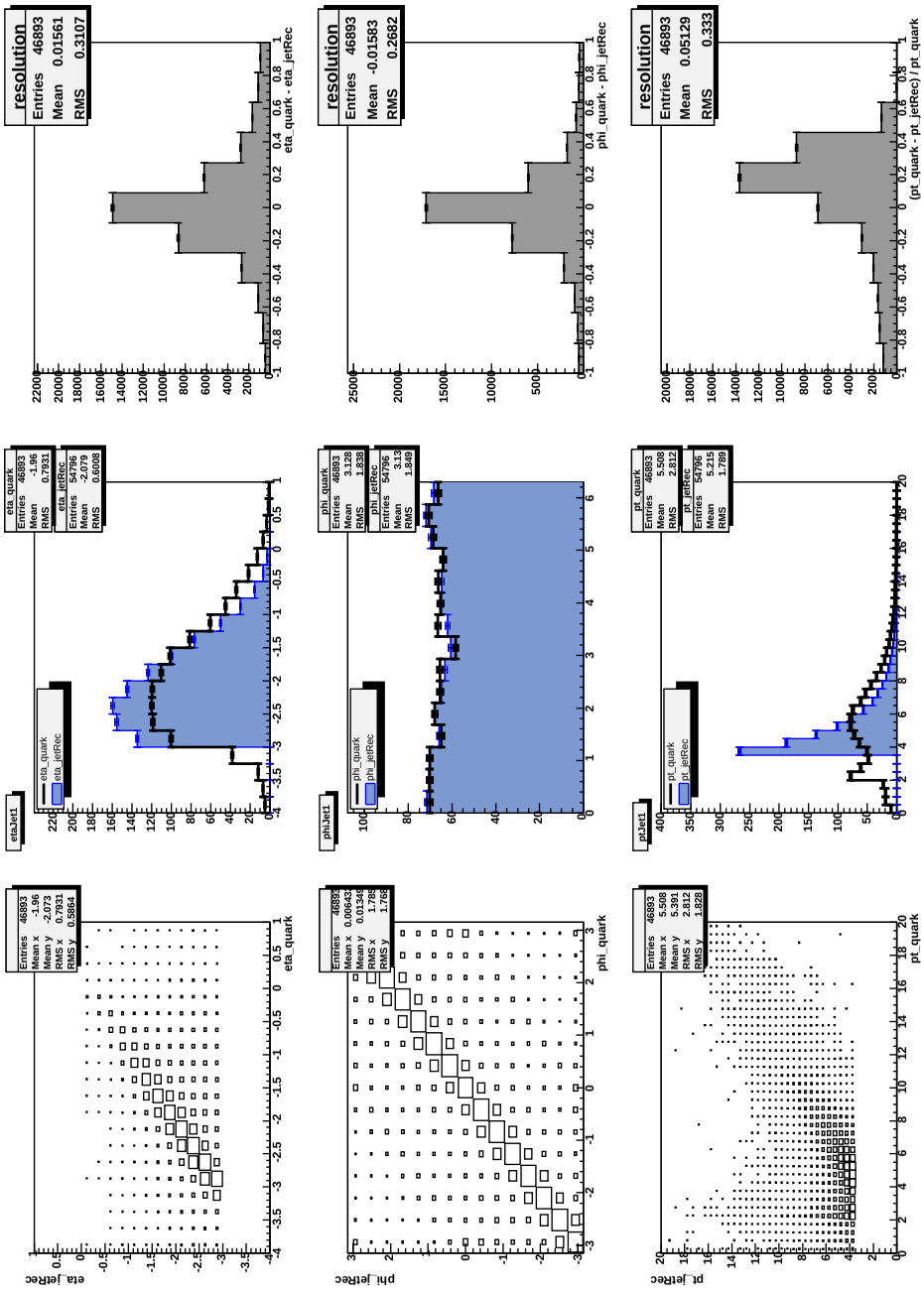

Figure 8.12: Correlation in η^*, ϕ^* and $p_\perp^*$ of the jet with the lower $p_\perp^*$ at the reconstructed level with the corresponding parton in the two gluon exchange Monte Carlo.

Chapter 9

Description of the Data with the Monte Carlo

9.1 Description of the Basic Kinematic Quantities

Comparison of the basic kinematic variables with both Monte Carlo predictions is displayed in figure 9.1. Q^2 and y are well described by both models using the electron method for the reconstruction.

9.1.1 The z Coordinate of the Primary Vertex

Figure 9.1 shows a good agreement in the z_{vertex} distribution. However, both Monte Carlo event samples required a small modification in order to exhibit such an agreement. The original distribution of the Monte Carlo events is slightly shifted in its mean value from what is seen in the data. The z_{vertex} distribution is produced during the detector simulation and has nothing to do with the physics model implemented in the Monte Carlo generator. The description is improved by *reweighting* the Monte Carlo events. The distributions of the data and the Monte Carlo were fitted with a gaussian. A ratio of these as a function of z component of the simulated vertex was applied as a weight for all Monte Carlo events. Thus every distribution gained from the Monte Carlo samples are reweighted according to the z_{vertex}.

9.1.2 The $\sum(E - p_z)$ of the Final State

Value of the $\sum(E - p_z)$ at the generator level equals to twice the initial electron energy. The observed smearing at the detector level is a result of the detector response. Neither of the Monte Carlo models gives a satisfactory description of the data. It is probably caused by insufficient hadronic final state calibration in its longitudinal component.

9.2 The Scattered Electron Properties

An agreement in the scattered electron properties is essential in the presented analysis. The scattered electron energy E_e, angles θ_e and ϕ_e, and the distance $d_{cluster-beam}$ are displayed in figure 9.2.

The energy of the scattered electron is extracted from the response of the cells in the SPACAL. Not all of the SPACAL cells were properly working during the whole running period. Events where the scattered electron deposits energy in these cells, so-called *dead cells*, must be dropped out from the data sample in order to preserve the high precision of the scattered electron energy measurement. The same has to be done also in the Monte Carlo sample to maintain the good description of the data. Excluding of the dead cells is reflected in the ϕ_e distribution that is not then perfectly uniform.

Both Monte Carlo models describe the scattered electron well.

9.3 Description of the Diffractive Variables

Figure 9.3 shows the comparison of the diffractive quantities η_{max} and $x_{I\!P}$. The resolved pomeron model reproduces the shapes retrieved from the data, whereas the distributions produced by the two gluon exchange model deviate from the desired shapes. This is probably caused by the choice of the gluon densities used in the Monte Carlo generator. Different gluon densities influence the $x_{I\!P}$ distribution in distinct ways, as mentioned in section 8.1. Another possibility is that the two gluon exchange model is not suitable for description of such events as analysed here.

9.3.1 The Forward Detectors

In section 6.3 were mentioned cuts on numbers of hits in the forward detectors[1]. These are ones of the cuts responsible for diffractive nature of analysed processes. They veto any hadronic activity between X and the proton system Y, and are applied together with the cut on η_{max} to ensure a presence of a rapidity gap. Using the RAPGAP Monte Carlo generator one can be sure that all generated events are diffractive.

When comparing the activity in the forward detectors in the data and in the Monte Carlo it is necessary to add an electronic noise to the hit distribution in the Monte Carlo in order to receive a good description of the data. It is not included in the H1 detector simulation and has to be determined from random trigger files for the same running period as under study in the analysis. Then the data are well described by the Monte Carlo.

The electronic noise was not added to the Monte Carlo hit distributions in this analysis. This procedure is needed only for purposes of measurement

[1]Forward Muon Detector and Proton Remnant Tagger.

of the cross section. That is not the case here.

9.4 Description of the Jet Variables

Figure 9.4 shows general characteristics of the dijet production: the multiplicity of the jets, $\Delta\phi^*$ of the two jets, transverse momentum balance of the two jets and the azimuthal angle ϕ^* of the jet plane.

The multiplicity is well described by both Monte Carlo samples.

The two jets form the jet-plane in the $\gamma^* p$ centre-of-mass system. Having only these two jets in the hadronic final state system X, they would head exactly in the opposite direction and would compensate each other's transverse momenta. As the inclusive dijet production is under study in this analysis, the system X consists of some other final states that do not contribute to the two jets. These form the low-energetic jets mentioned in the previous paragraph and cause a slight deflection from the back-to-back alignment as well as bias the balance of the transverse momenta. This explains the shape that is observed in the histogram. Both Monte Carlo give a good description of the transverse momentum balance seen in the data.

The peak around back-to-back direction shown in figure 9.4 is broader for the Monte Carlo models than the data express. It is important to note here that this is generally known defect of RAPGAP Monte Carlo.

The azimuthal angle in the $\gamma^* p$ frame of the jet plane is well described by both Monte Carlo models. Note that no asymmetry is seen either in the data or in any of the two models, the distributions are uniform.

Figures 9.5 and 9.6 display general characteristics of the first and the second jet in transverse momentum, respectively. In these figures one can see the transverse momentum distribution, η^* and ϕ^* distributions, and the multiplicity of particles in the jet.

Note that the latter quantity is described better by the resolved pomeron model. All the quantities are in reasonable agreement with both Monte Carlo samples.

9.5 Description of the Dijet Kinematics

Figure 9.7 shows the comparison of the dijet kinematics, β and $\xi_{I\!P}$, mass of the hadronic final state, M_X, and the invariant mass of the dijet system, M_{12}. The dijet kinematic variables are derived using these two masses, thus any disagreement in the mass distributions results in a disagreement in the dijet kinematic variables.

Kinematic quantity β is well described by the resolved pomeron Monte Carlo. The two gluon exchange Monte Carlo does not give such a good description. In case of $\xi_{I\!P}$ none of the two Monte Carlo models describe the

data. Both models give qualitatively different distributions, from which the resolved pomeron Monte Carlo resembles the data more.

The invariant mass of the dijet system is correctly reproduced by the both models, whereas the hadronic final state mass reserves a slight improvement. The disagreement in M_X can be improved by applying some so-called *correction factors*. These factors shift the reproduced mass to the right values and repress the insufficient calibration of the relevant detector components. The p_T-*compensation*, shown in figure 9.8, displays the difference between the transverse momentum of the scattered electron and the transverse momentum of the hadronic final state X, which should be balanced according to the conservation laws[2]. As it has the mean value at 0, no correction factors have to be applied concerning the transversal component. However, the p_T-compensation does not tell anything about the longitudinal component of the hadronic final state. As already mentioned, the $\sum(E-p_z)$ distribution points to its not precise measurement, but no correctoin factors can be determined out of that.

Other thing that might help to improve the agreement of the dijet kinematic variables is a *reweighting* of the Monte Carlo hadronic final state mass. It would then be in a perfect agreement with the data and such change could affect in a positive way the derived variables β and $\xi_{I\!P}$. However, this is not the case in this analysis. Reweighting of the mass M_X results in worsening of the agreement in dijet invariant mass M_{12}, thus the description of the dijet kinematic variables remains insufficient.

9.6 Resolved and Direct Processes

Figure 9.8 also includes comparison of x_γ. This quantity can be calculated as follows

$$x_\gamma = \frac{(E-p_z)_{jet_1} + (E-p_z)_{jet_2}}{\sum_{i\in X}(E-p_z)_i}, \tag{9.1}$$

and physically refers to a fraction of the virtual photon momentum that enters the hard interaction. Processes where no structure of the photon is assumed are referred to as *direct*, and are characterised by the value of $x_\gamma = 1$. Processes involving the photon structure contain so-called photon remnant in the final state. These are called *resolved*, and are demarked by the value of $x_\gamma < 1$.

Only the direct processes are simulated in both Monte Carlo models. The value of x_γ is not 1 sharp because of the reconstruction uncertainties and the jet algorithm resolution. As the data are reasonably described by both samples, one can conclude that the resolved processes are not present

[2]The p_T-compensation does not take into account the proton system Y that vanishes in the beam-pipe undetected with a small transverse momentum. Thus the balance, as defined above, cannot be prefect even in case of ideal detector conditions.

in the data sample as well. Thus, no other Monte Carlo files had to be added.

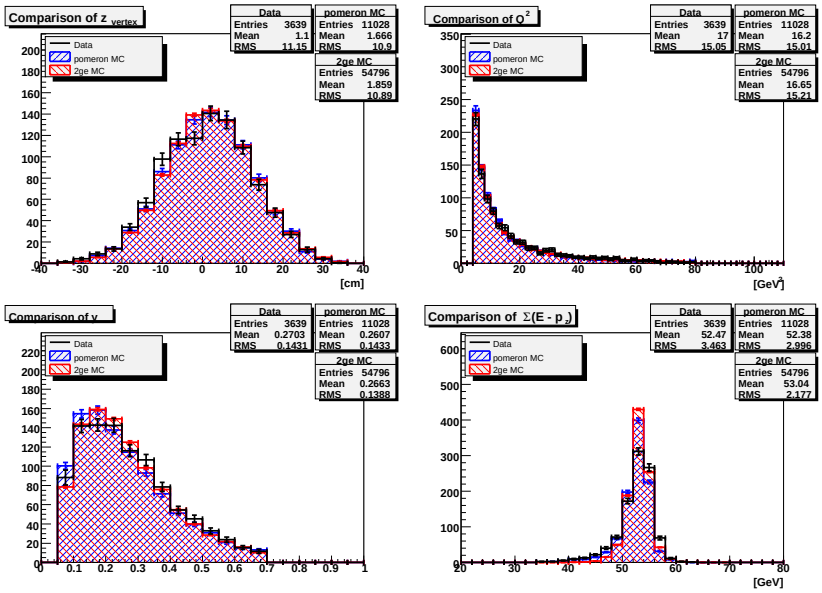

Figure 9.1: Description of z_{vertex}, Q^2, y and $\sum(E-p_z)$ by both Monte Carlo models.

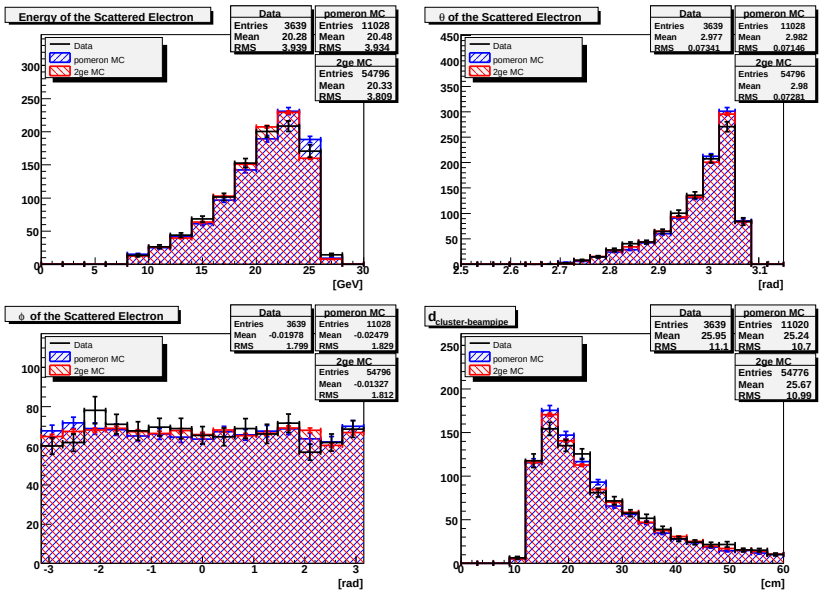

Figure 9.2: Description of the scattered electron properties E_e, θ_e, ϕ_e and $d_{cluster-beam}$ by both Monte Carlo models.

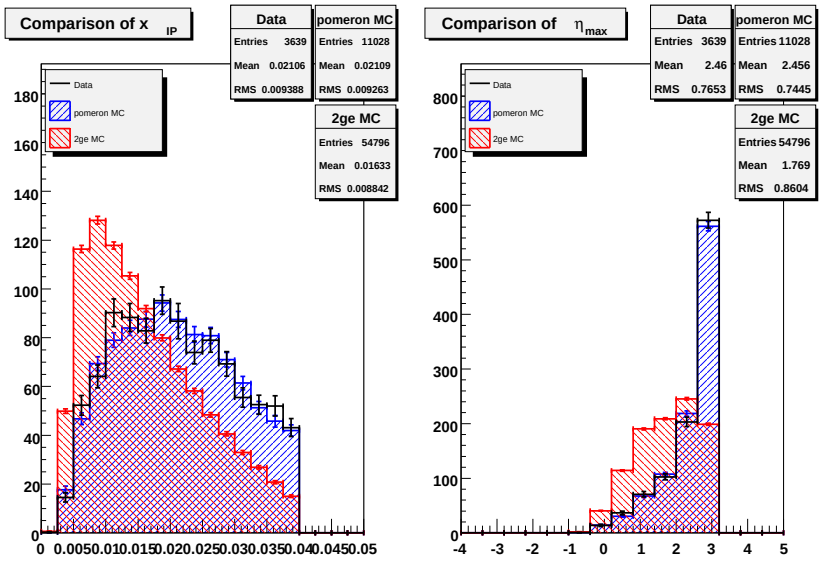

Figure 9.3: Description of the diffractive variables $x_{I\!P}$ and η_{max} by both Monte Carlo models.

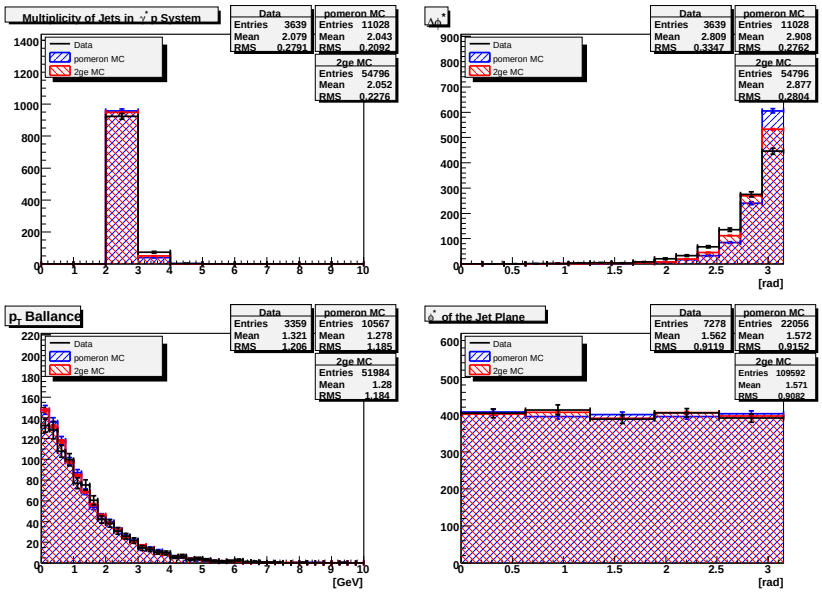

Figure 9.4: Multiplicity of the jets found in $\gamma^* p$ centre-of-mass system, $\Delta\phi^*$, transverse momentum balance of the jets, azimuthal angle ϕ^* of the jet plane.

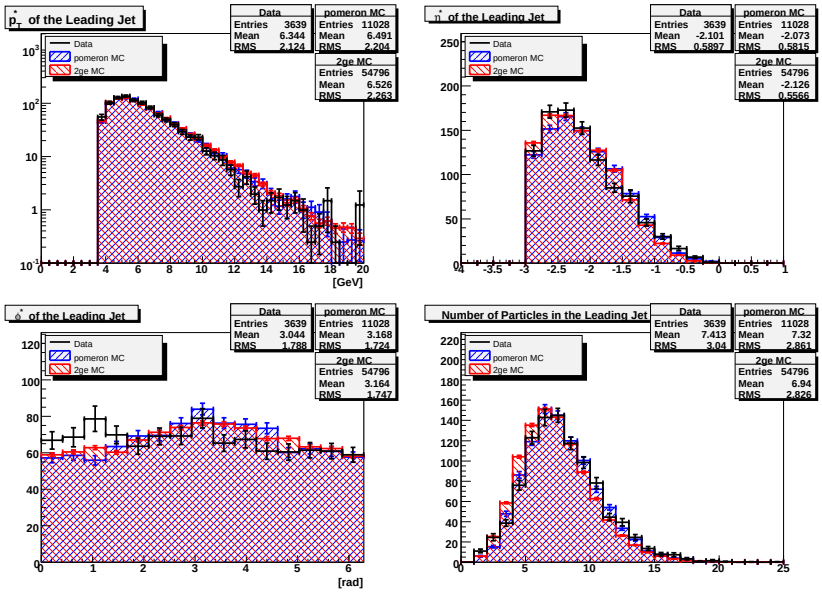

Figure 9.5: Description of the jet with the higher p_T by both Monte Carlo models. Transverse momentum, η^*, ϕ^* and multiplicity of particles within the jet are displayed.

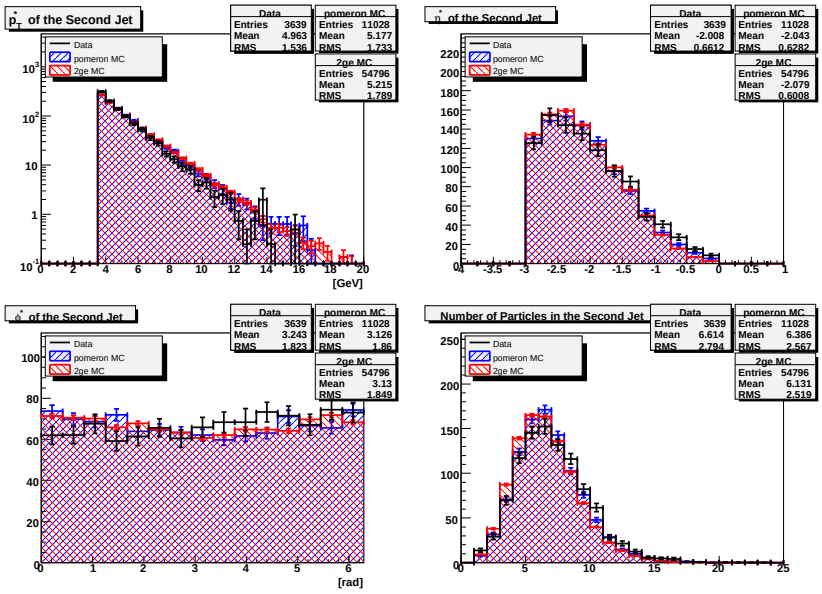

Figure 9.6: Description of the properties of the jet with the lower p_T by both Monte Carlo models. Transverse momentum, η^*, ϕ^* and multiplicity of particles within the jet are displayed.

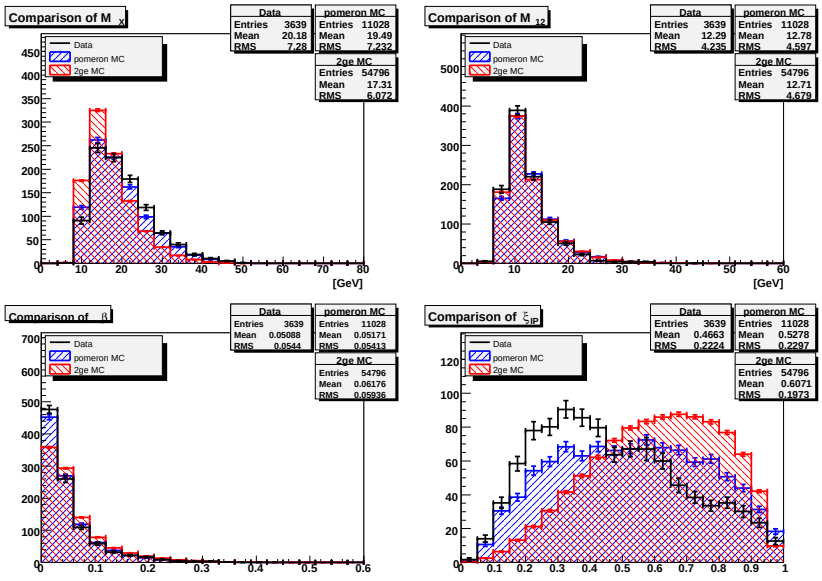

Figure 9.7: Description of invariant masses M_X, M_{12} and of dijet kinematic quantities β and $\xi_{I\!P}$.

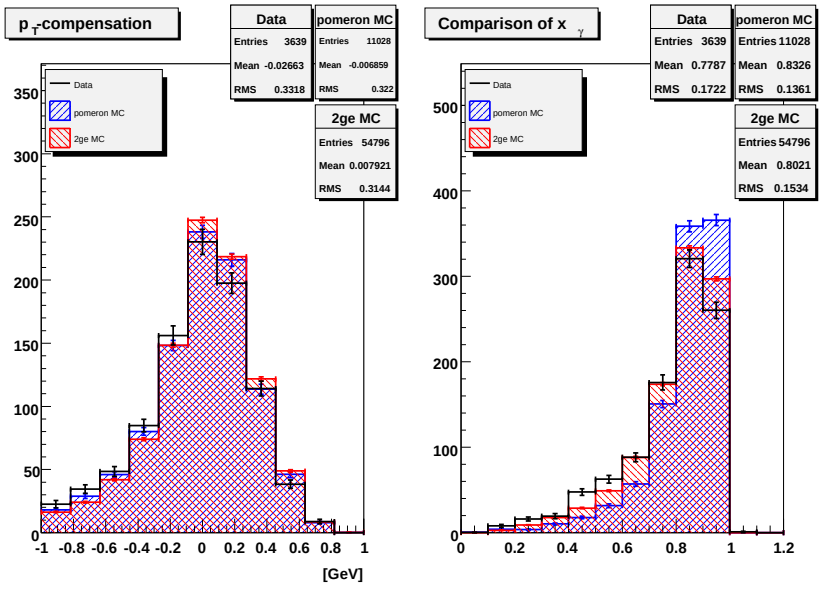

Figure 9.8: p_T-compensation and x_γ in the data and both Monte Carlo samples.

Chapter 10

The Azimuthal Asymmetry

In principle, the different dependencies upon ϕ^* mentioned in section 3.4 might help to discriminate between the two models: the exchange of a colour singlet two-gluon state and the single gluon exchange in the boson-gluon-exchange model.

As already mentioned in section 9.4 azimuthal asymmetry is seen neither in the data nor in any of the two Monte Carlo samples. This was shown in figure 9.4 which illustrates the azimuthal dependence of the jet plane taking into account all the events that pass the analysis cuts. It is important to note that the azimuthal asymmetry predictions concern only the boson-gluon-fusion and the $q\bar{q}$ processes. All the remaining processes are treated as a background. The signal process in the resolved pomeron Monte Carlo forms majority of the events (see figure 8.2). In the two gluon exchange model, the yield of the signal process is negligible in comparison with the yield of the background process (see figure 8.4). There is a hope to find some kinematical region where the production of the signal process is emphasised.

Tables 7.1, 8.5 and 8.8 show the final statistics of the data and both the Monte Carlo samples that fulfil all the analysis cuts. This analysis is performed on a rather small statistics in the data and the resolved pomeron Monte Carlo. And the restrictions to certain kinematical regions decrease the statistics even more. The insufficient statistics is treated in the following way:

- As seen in figure 9.4 the two jets head in the opposite directions in the $\gamma^* p$ system, and together with the incoming proton form a plane. Thus the azimuthal angle ϕ^* of this plane with respect to the lepton plane can be described by both azimuthal angles of the two jets. Hence both the angles are plotted in one histogram.

- Bearing in mind the symmetries of the calculated azimuthal distributions outlined in figure 3.10, the range of the plotted distributions can be restricted to the interval from 0 to $\pi/2$.

- And finally, in order to reduce the errors in the most effective way, it is advisable to divide the histograms only into two bins. Then a dominant signal in the bin from 0 to $\pi/4$ denotes the BGF process asymmetry, whereas a dominant signal in the bin from $\pi/4$ to $\pi/2$ reflects the $q\bar{q}$ process asymmetry.

10.1 The Azimuthal Asymmetry in the Monte Carlo

Different quantities at the generator level were examined in detail in order to find an interval within their domain range where the asymmetry signal would be visible, taking into account the statistical errors. Resulting regions are illustrated in figure 10.1 and listed in table 10.1 along with the number of contributing events and the relative content of the boson-gluon-fusion process. It is clear that the observed asymmetry arise from the signal process.

In case of the two gluon exchange Monte Carlo, the most crucial fact is the negligible ratio of the yield of the signal process to the yield of the background process (see figure 8.4). A stand-alone $q\bar{q}$ process exhibits very clear asymmetry signal (see figure 10.7). Unfortunately, it is almost completely repressed by the dominant contribution of the $q\bar{q}g$ process. Again, different quantities were studied for purpose of finding the range where the contribution of the signal process would be emphasised. Results can be found in table 10.2 and in figure 10.2. However, the only variables exhibiting a region of significant $q\bar{q}$ process production are the dijet kinematic quantities β and $\xi_{I\!P}$. The identified region of β close to 1 perfectly confirms the theoretical predictions outlined in section 3.4. The low percentage of the signal process shown in table 10.2 points out that the experimental evidence of the $q\bar{q}$ asymmetry is difficult to observe. The asymmetry is given by the signal process only in case of the region defined by the cut on β!

In both Monte Carlo samples at the parton level there are some regions where the asymmetry coming from the signal process is visible (although there is only one such region found in the two gluon exchange Monte Carlo sample). The question is how does it reflect at the reconstructed level, whether the asymmetry of the signal process can also be seen there. The transition between these two levels is affected by reconstruction (smearing due to detector response). The variables that are reconstructed with high resolution are assumed to define similar regions of azimuthal asymmetry at the reconstructed level, as they do at the generator level. Those quantities that are not well correlated between the two levels are not being taken into account at the reconstructed level any more. These are the dijet kinematic quantities β and $\xi_{I\!P}$ (see figure 8.7). Unfortunately the most significant yield of the $q\bar{q}$ process is exhibited in the region determined by the cuts on these variables. Hence, in case of the two gluon exchange model the asymmetry of

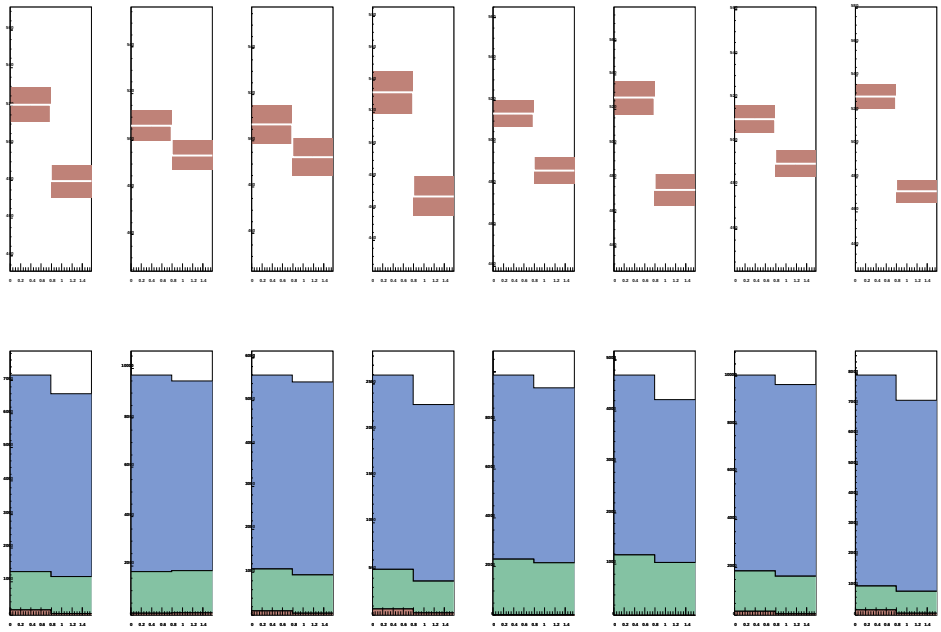

Figure 10.1: Regions where the azimuthal asymmetry is clearly visible at the parton level in the resolved pomeron model. The upper histograms show the asymmetry along with the statistical errors. Note that the vertical axis does not begin at 0. The lower histograms depicts the relative contributions of particular processes simulated in the model. These are QPM, QCDC and BGF, from the bottom respectively. Both histograms in one column depict the same region. Plotted regions correspond to those listed in table 10.1.

Region	Events in MC	Contribution of BGF
$4. < Q^2 < 8.$	3560	82.2%
$0.2 < y < 1.$	7331	81.3%
$16. < M_X < 22.$	4354	81.8%
$18. < M_{12} < 40.$	1840	82.2%
$6. < p_\perp^{jet1} < 30.$	7235	76.8%
$6. < p_\perp^{jet2} < 8.$	3372	75.1%
$0.01 < \beta < 0.05$	7430	82.3%
$0.5 < \xi_{I\!P} < 1.$	6003	88.3%

Table 10.1: Regions where the azimuthal asymmetry is clearly visible at the parton level in the resolved pomeron model.

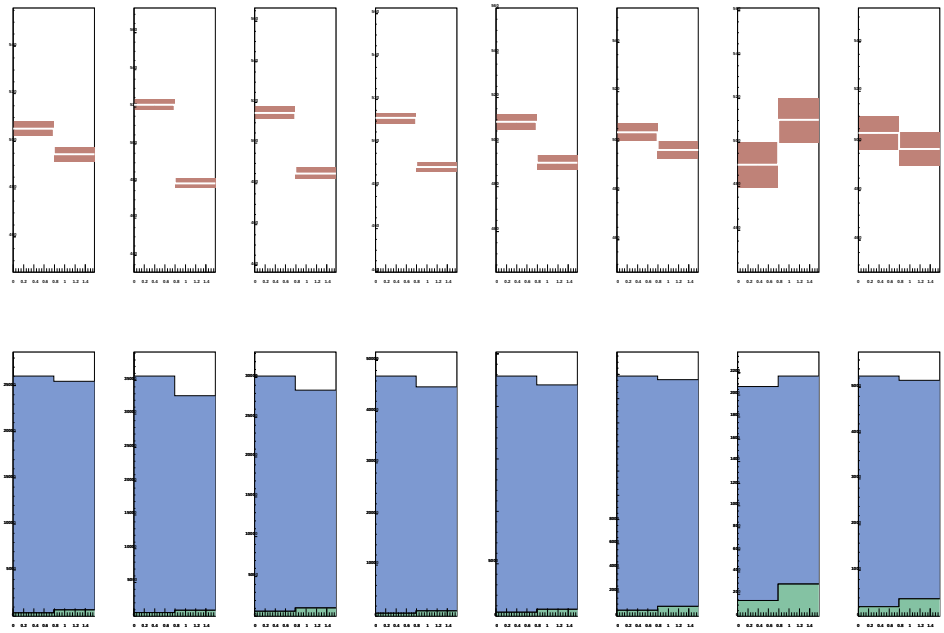

Figure 10.2: Regions of stronger contribution of the $q\bar{q}$ process at the parton level in the two gluon exchange model. The upper histograms show the asymmetry along with the statistical errors. Note that the vertical axis does not begin at 0. The lower histograms depicts the relative contributions of particular processes simulated in the model. These are $q\bar{q}$ and $q\bar{q}g$, from the bottom respectively. Both histograms in one column depict the same region. Plotted regions correspond to those listed in table 10.2.

Region	Events in MC	Contribution of $q\bar{q}$
$16. < Q^2 < 80.$	30720	2.0%
$0. < y < 0.2$	40811	2.1%
$0. < M_X < 16.$	37112	2.8%
$0. < M_{12} < 13.$	53744	1.8%
$4.5 < p_\perp^{jet1} < 6.$	27328	2.3%
$4.5 < p_\perp^{jet2} < 8.$	25811	3.3%
$0.2 < \beta < 1.$	4152	10.2%
$0.8 < \xi_{I\!P} < 1.$	7950	5.6%

Table 10.2: Regions of stronger contribution of the $q\bar{q}$ process at the parton level in the two gluon exchange model.

the signal process cannot be studied at the reconstructed level in this way. As seen in the figure 8.7 there is no statistics in the region $\beta \to 1$ at the reconstructed level anyway.

Thus the same probe of the various kinematic quantities as at the parton level was performed as well at the reconstructed level. Regions where the azimuthal distribution exhibits a clear asymmetry, taking into account statistical errors, are depicted in figures 10.3, 10.4 and listed in tables 10.3, 10.4. These include also a comparison with the data. Note that the regions found at the reconstructed level do not correspond to those discovered at the generator level. In all the regions depicted in figure 10.3 and table 10.3 one can see a clear asymmetry signal coming from the boson-gluon-fusion process. In case of the two gluon exchange model (figure 10.4 and table 10.4) there is no region with the significant yield of the signal process based on the cut on some well reconstructed variable.

10.2 The Azimuthal Asymmetry in the Data

The statistics in the Monte Carlo ought to be much larger than that in the data. It is to ensure that some region found in the data, that exhibits some specific shape of a distribution of one particular quantity, would be well described by the Monte Carlo sample taking into account the statistical errors. In this analysis, the statistics in the two-gluon-exchange sample is sufficient enough. In case of the resolved pomeron Monte Carlo the statistics should be larger in order to give a satisfactory description.

Let us have a look at figures 10.3, 10.4 and tables 10.3, 10.4 once more. These also demonstrate behaviour of the data. All regions in both Monte Carlo samples describe the data within 3σ. The two gluon exchange model gives slightly better description.

Also the data sample was studied in a similar way as the Monte Carlo. Concerning the low statistics, a point was to find a region defined by some cut on particular variable where the effect of the asymmetry would be larger than the statistical errors. The results are listed in tables 10.5, 10.6 and figures 10.5, 10.6 compared with the resolved pomeron Monte Carlo and the two gluon exchange Monte Carlo, respectively. Again, all regions are described by both Monte Carlo samples within 3σ. And again, the two gluon exchange model gives slightly better description. However, the amount of $q\bar{q}$ events is so small that the azimuthal dependence expressed by this process cannot be confirmed experimentally.

10.3 Summary and Outlook

From all the tables and plots presented in this chapter it is clear that, according to the low statistics of the data sample, no conclusions based

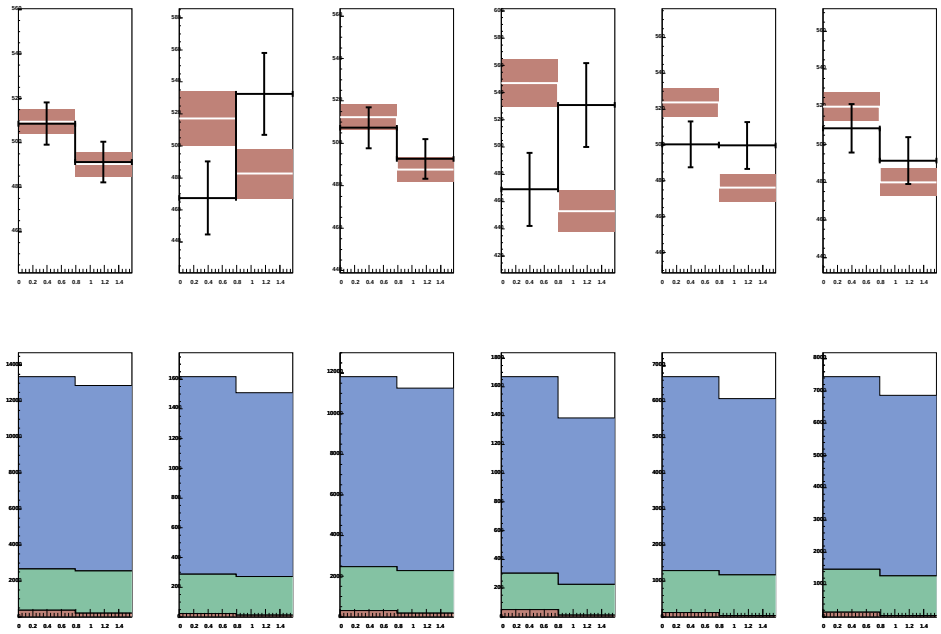

Figure 10.3: Regions where the azimuthal asymmetry is clearly visible at the reconstructed level in the resolved pomeron model. The upper histograms show the asymmetry along with the statistical errors in comparison with the data. Note that the vertical axis does not begin at 0. The lower histograms depicts the relative contributions of particular processes simulated in the model. These are QPM, QCDC and BGF, from the bottom respectively. Both histograms in one column depict the same region. Plotted regions correspond to those listed in table 10.3.

Region	Events in Data	Events in MC	Contribution of BGF
$4. < Q^2 < 100.$	3639	9806	80.2%
$0.45 < y < 1.$	483	1167	82.1%
$12. < M_X < 50.$	3317	8604	79.5%
$18. < M_{12} < 40.$	339	1126	82.6%
$6. < p_\perp^{jet1} < 30.$	1715	4795	80.7%
$4.5 < p_\perp^{jet2} < 30.$	1813	5352	80.8%

Table 10.3: Regions where the azimuthal asymmetry is clearly visible at the reconstructed level in the resolved pomeron model. Cuts are applied only on well reconstructed variables.

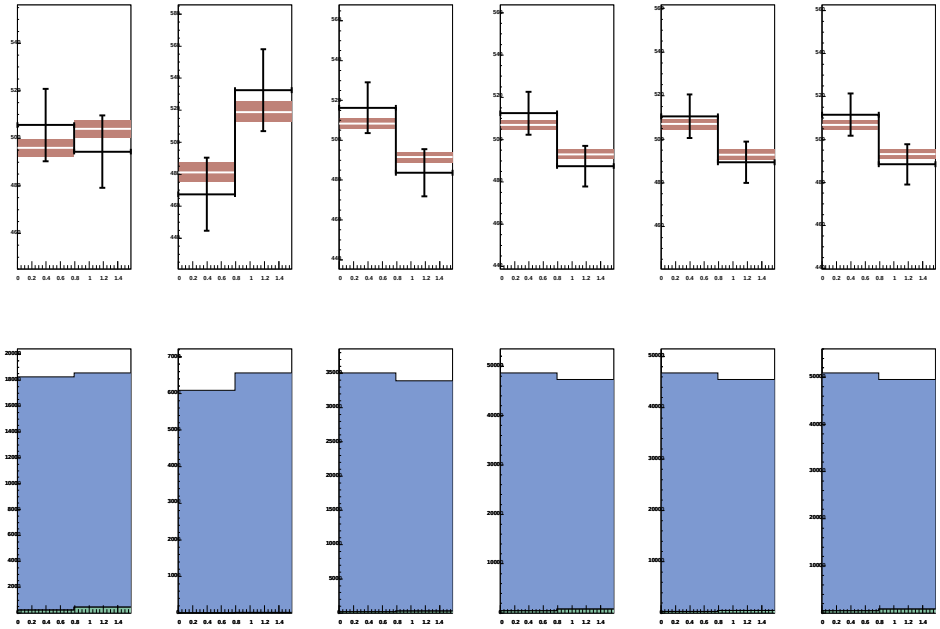

Figure 10.4: Regions where the azimuthal asymmetry is clearly visible at the reconstructed level in the two gluon exchange model. The upper histograms show the asymmetry along with the statistical errors in comparison with the data. Note that the vertical axis does not begin at 0. The lower histograms depicts the relative contributions of particular processes simulated in the model. These are $q\bar{q}$ and $q\bar{q}g$, from the bottom respectively. Both histograms in one column depict the same region. Plotted regions correspond to those listed in table 10.4.

Region	Events in Data	Events in MC	Contribution of $q\bar{q}$
$16. < Q^2 < 80.$	1283	21709	1.9%
$0.45 < y < 1.$	483	6543	0.3%
$12. < M_X < 22.$	2036	37054	0.7%
$0. < M_{12} < 18.$	3299	54125	1.3%
$4.5 < p_\perp^{jet1} < 30.$	3093	50474	1.0%
$3.5 < p_\perp^{jet2} < 8.$	3457	56433	1.3%

Table 10.4: Regions where the azimuthal asymmetry is clearly visible at the reconstructed level in the two gluon exchange model. Cuts are applied only on well reconstructed variables.

Region	Events in Data	Events in MC	Contribution of BGF
$0.3 < y < 0.45$	901	2108	80.1%
$0.45 < y < 1.$	483	1167	82.1%
$12. < M_X < 22.$	2036	5757	78.3%
$0. < M_{12} < 13.$	2414	6210	79.8%
$18 < M_{12} < 40.$	339	1126	82.6%
$4.5 < p_\perp^{jet1} < 6.$	1378	3594	80.4%
$3.5 < p_\perp^{jet2} < 6.$	2960	7620	80.1%
$8. < p_\perp^{jet2} < 30.$	182	711	79.2%

Table 10.5: Regions where the azimuthal asymmetry is clearly visible in the data in comparison with the resolved pomeron model. Cuts are applied only on well described variables.

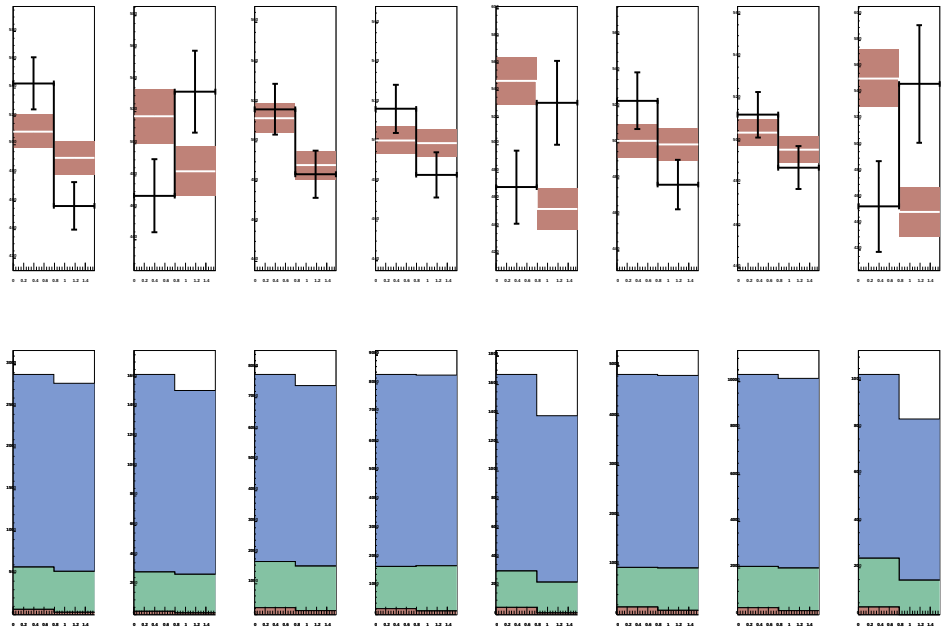

Figure 10.5: Regions where the azimuthal asymmetry is clearly visible in the data compared with the resolved pomeron model. The upper histograms show the asymmetry along with the statistical errors. Note that the vertical axis does not begin at 0. The lower histograms depicts the relative contributions of particular processes simulated in the model. These are QPM, QCDC and BGF, from the bottom respectively. Both histograms in one column depict the same region. Plotted regions correspond to those listed in table 10.5.

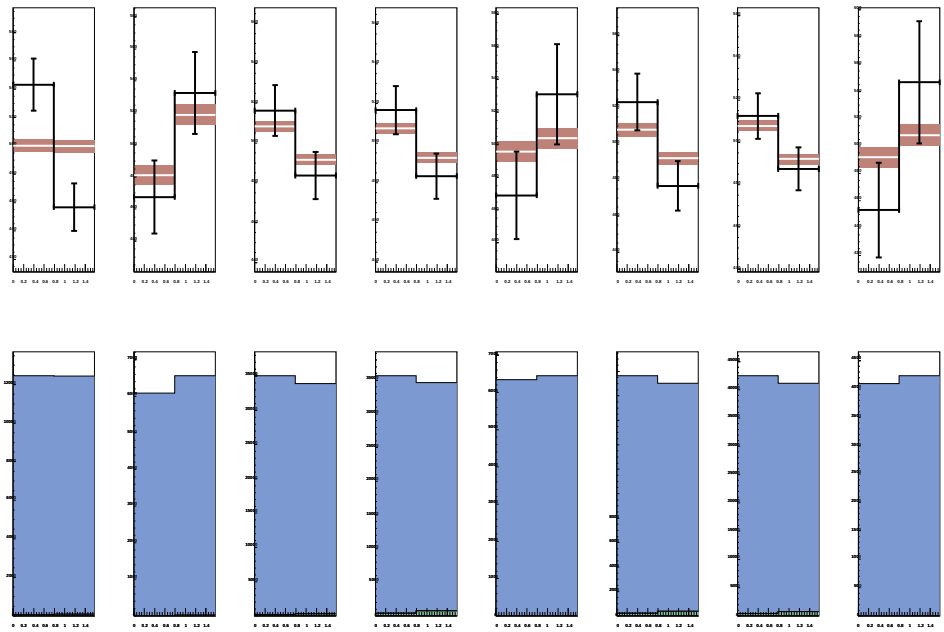

Figure 10.6: Regions where the azimuthal asymmetry is clearly visible in the data compared with the two gluon change model. The upper histograms show the asymmetry along with the statistical errors. Note that the vertical axis does not begin at 0. The lower histograms depicts the relative contributions of particular processes simulated in the model. These are $q\bar{q}$ and $q\bar{q}g$, from the bottom respectively. Both histograms in one column depict the same region. Plotted regions correspond to those listed in table 10.6.

Region	Events in Data	Events in MC	Contribution of $q\bar{q}$
$0.3 < y < 0.45$	901	13142	0.5%
$0.45 < y < 1.$	483	6543	0.3%
$12. < M_X < 22.$	2036	37054	0.7%
$0. < M_{12} < 13.$	2414	40505	1.6%
$18 < M_{12} < 40.$	339	6529	0.2%
$4.5 < p_\perp^{jet1} < 6.$	1378	22152	1.5%
$3.5 < p_\perp^{jet2} < 6.$	2960	47622	1.5%
$8. < p_\perp^{jet2} < 30.$	182	4253	0.2%

Table 10.6: Regions where the azimuthal asymmetry is clearly visible in the data compared with the two gluon exchange model. Cuts are applied only on well described variables.

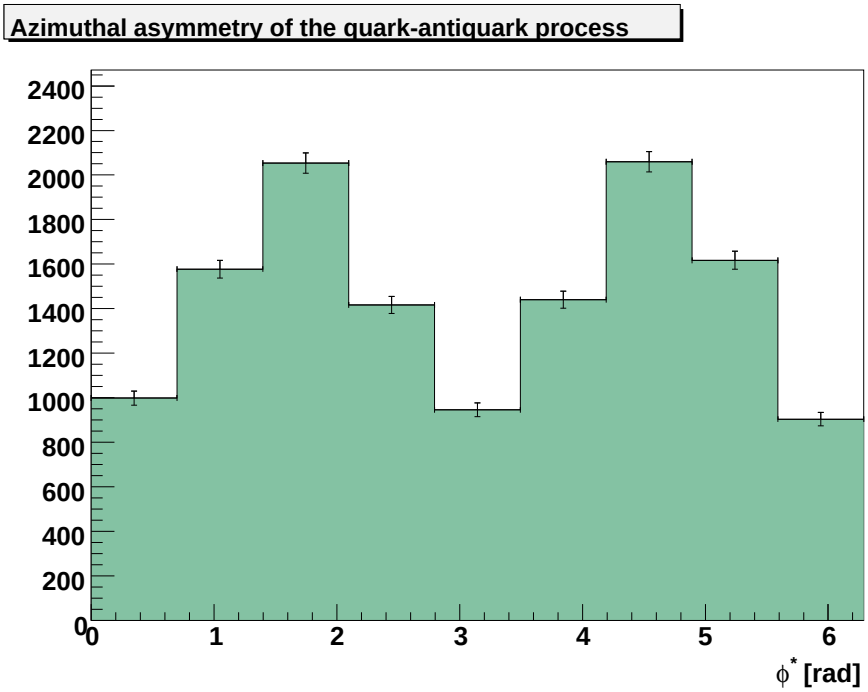

Figure 10.7: Clear azimuthal asymmetry signal of the $q\bar{q}$ process.

on the comparison of the azimuthal angle of the jet plane can be drawn. The insufficient statistics results in large statistical errors that shade the asymmetry signal. Moreover, it is necessary to point out that none of the distributions shown includes the systematic errors. These would suppress the significance of the observed asymmetry effect even more.

Concerning the resolved pomeron Monte Carlo it is also rather difficult to find a region of clear boson-gluon-fusion asymmetry signal with the statistics available. For a further study it is proposed to generate more events and to examine the azimuthal asymmetry with a higher statistics in more detail.

In case of the two gluon exchange Monte Carlo sample the statistics is sufficient enough to investigate the asymmetry behaviour at the generator level. Due to the high statistics, more complex cuts can be performed in order to find regions where the contribution of $q\bar{q}$ process would not be so negligible. A cut on $\Delta\eta^*$ of the jets is advised in order to reduce the contribution of the $q\bar{q}g$ events. Events where one jet emerges from the both quark and antiquark and the other jet comes out from a gluon express slightly different $\Delta\eta^*$ distribution then events where the gluon contributes to one of the two jets evolving from quark and antiquark each. [21]

The asymmetry of the $q\bar{q}$ process is clearly observable in the Monte

Carlo sample when not taking into account the dominant contribution of the background $q\bar{q}g$ process. Figure 10.7 displays the azimuthal angle of the jet plane in the $\gamma^* p$ centre-of-mass system of all the $q\bar{q}$ events in the final Monte Carlo sample. No cuts restricting the phase space to some particular region have been applied here. A majority of the plots shown in this chapter exhibit an asymmetry that is just opposite. It case of the resolved pomeron Monte Carlo it is exactly what one expects from the boson-gluon-fusion process. But in the two gluon exchange model the final azimuthal signal is in most cases the same. Thus there is no sensitivity to the $q\bar{q}$ asymmetry signal observed. It is due to a negligible ratio of the yield of the signal process to the yield of the background process. Therefore the fact that the two gluon exchange model describes the azimuthal distributions slightly better is of no significance. Nothing can be said about the signal process because there is no experimental evidence of its azimuthal asymmetry. Moreover, other quantities then the azimuthal angle ϕ^* are better desribed by the resolved pomeron model.

Chapter 11

Summary

A dijet production in diffractive deep-inelastic scattering has been studied in order to judge between two distinct theoretical approaches of describing the diffractive processes: the resolved pomeron model on one hand, and the two gluon exchange model on the other. Calculations lead to a different azimuthal dependence of the outgoing partons in basic processes present in both models. As jets inherit the kinematical properties of original partons, dijet events serve as a suitable instrument to decide in favour of one of the introduced approaches.

Events in the kinematic region of 4. $\mathrm{GeV}^2 < Q^2 < 80.\ \mathrm{GeV}^2$, $0.05 < y < 0.7$, $x_{I\!P} < 0.05$, exhibiting a clear rapidity gap with $\eta_{max} < 3.2$, and containing at least two jets evolving in the range of pseudorapidity $-3. < \eta^* < 0.$ in the $\gamma^* p$ centre-of-mass system, with the transverse momenta $p_T^* > 3.5$ in the same system were compared with the predictions of both mentioned models. RAPGAP Monte Carlo generator was used to produce required event samples. Data acquired in the years 1999, 2000 were analysed. The main results are listed below:

- Due to the insufficient statistics in the data sample, no conclusions based on the azimuthal asymmetry were drawn. The distributions observed in the data are in good agreement with both Monte Carlo models, taking into account the statistical errors.
- The resolved pomeron Monte Carlo describes the data reasonably well.
- The diffractive quantities $x_{I\!P}$ and η_{max} in the two gluon exchange Monte Carlo do not describe the data at all. This kind of disagreement can be caused by wrong choice of the gluon densities. Study of the different gluon densities and their influence on $x_{I\!P}$ lies beyond the scope of this analysis.
- In case of the two gluon exchange model there were substantial discrepancies in dijet kinematic variables. These are derived from the

invariant mass of the system X. Neither applying of the correction factor to this mass, nor its reweighting did lead to any improvement. However, it is left for the further study to show whether the Monte Carlo can be fine-tuned by changing some of its initial parameters, or whether the two gluon exchange model is just not suitable for this kind of analysis.

- The ratio of the signal process yield to the background process yield in the two gluon exchange model is almost negligible. Scanning the phase space, certain regions where the signal process production is emphasised were pointed out. Unfortunately, the cross section in such regions is insignificantly small. Further cuts that would amplify the ratio were proposed.

Higher statistics in the data is needed in order to perform this analysis with desired results. Nevertheless, it is questionable whether there exists experimentally accessible kinematic region where one can investigate the azimuthal asymmetry of the $q\bar{q}$ process in the two gluon exchange approach.

Bibliography

[1] H1 Collaboration: The H1 Detector at HERA, Internal Report DESY H1-96-01, 1996.

[2] T. Nicholls *et al.*, Nucl. Instrum. Methods A374 (1996) 149.

[3] ZEUS Collaboration: Measurements of total and partial photon proton cross sections at 180 GeV center of mass energy, Z. Phys. C 63 (1994) 391-408.

[4] H1 Collaboration, Observation of hard processes in rapidity gap events in γp interactions at HERA, Nucl. Phys. B 435 (1995) 3-20.

[5] ZEUS Collaboration: Observation of hard scattering in photoproduction events with a large rapidity gap at HERA, Phys. Lett. B 346 (1995) 399-414.

[6] H1 Collaboration: Diffractive dissociation in photoproduction at HERA, Z. Phys. C 74 (1997) 221-235

[7] ZEUS Collaboration: Observation of events with a large rapidity gap in deep inelastic scattering at HERA, Phys. Lett. B 315 (1993) 481-493.

[8] H1 Collaboration: Deep inelastic scattering events with a large rapidity gap at HERA, Nucl. Phys. B 429 (1994) 477-502.

[9] P. D. B. Collins: An Introduction to Regge Theory and High Energy Physics, Cambridge University Press, 1977.

[10] G. Ingelman, P. Schlein: Jet structure in high mass diffractive scattering, Phys. Lett. B 152 (1985) 256-260.

[11] UA8 Collaboration: Evidence for transverse jets in high-mass diffraction, Phys. Lett. B 211 (1988) 239-246.

[12] UA8 Collaboration: Evidence for a super-hard pomeron structure, Phys. Lett. B 297 (1992) 417-424.

[13] H1 Collaboration: First measurement of the deep-inelastic structure of proton in diffraction, Phys. Lett. B 348 (1995) 681-696.

[14] H1 Collaboration: A measurement and QCD analysis of the diffractive structure function $F_2^{D(3)}$, 28th International Conference on High Energy Physics, Warsaw, Poland, July 1996.

[15] J. Bjorken, Phys. Rev. 179 (1969) 1547.

[16] R. Feynman, Phys. Rev. Lett. 23 (1969) 1415.

[17] M. Gell-Mann, Phys. Lett. 8 (1964) 214.

[18] S. D. Ellis, D. E. Soper: Successive combination jet algorithm for hadron collisions, Phys. Rev. D 48 (1993) 3160-3166

[19] H. Jung: Monte Carlo Implementation of Diffraction at HERA, hep-ph/9809374v1

[20] J. Bartels, C. Ewerz, H. Lotter, M. Wüsthoff, M. Diehl: Quark-Antiquark Jets in DIS Diffractive Dissociation

[21] J. Bartels, H. Jung, M. Wüsthoff: Quark-Antiquark-Gluon Jets in DIS Diffractive Dissociation, Eur. Phys. J. C 11, 111-125 (1999)

[22] J. Bartels, C. Ewerz, H. Lotter, M. Wüsthoff: Azimuthal Distribution of Quark-Antiquark Jets in DIS Diffractive Dissociation

[23] S. Eidelman *et al.*: Review of Particle Physics, Physics Letters B 529, 1 (2004)

[24] H. Jung: The RAPGAP Monte Carlo for Deep Inelastic Scattering, http://www.desy.de/~jung/rapgap.html

[25] T. Anthonis: Multiplicity Structure of inclusive and diffractive deep-inelastic e^+p collisions at HERA, H1prelim-05-015

[26] R. Brun, F. Rademakers, Nucl. Instrum. Meth. A389, 81 (1997), available at http://root.cern.ch.

[27] The H1OO Group, available at https://www-h1.desy.de/icas/oop/.